A granular modeling method for non-uniform panel degradation based on I–V characterization and electroluminescence imaging

Martin Garaj [a,*], Henry Shu-Hung Chung [a], Sergiu Spataru [b], Alan Wai-Lun Lo [c], Huai Wang [d]

[a] Department of Electrical Engineering, City University of Hong Kong, Hong Kong
[b] Department of Photonics Engineering, Technical University of Denmark, Copenhagen, Denmark
[c] Department of Computer Science, Chu Hai College of Higher Education, Hong Kong
[d] Department of Energy Technology, Aalborg University, Aalborg, Denmark

ARTICLE INFO

ABSTRACT

A new model of photovoltaic (PV) panel is proposed. The model precisely replicates sub-cell level degradation, such as cracks and interconnect failures, and reproduces their effect at the panel level I–V characteristic. Moreover, a regression method is proposed, which infers the model's parameters from combination of electroluminescent (EL) image and degraded I–V characteristic. The combination of quantitative (EL image) and qualitative (I–V characteristic) enables to characterize the degradation of the cells embedded in the PV panel, without physical access to the cells. The proposed model and the regression problem is experimentally verified on a set of 3 single cell measurements and a set of 4 crystalline PV panels with various levels of degradation.

The Paris Agreement emphasizes *sustainable lifestyles and sustainable patterns of consumption and production* (Horowitz, 2016) as an appeal to governments to curb Greenhouse Gas emissions in an attempt to suppress climate change. Renewable energy sources are the answer for cleaner energy production, a field that is otherwise dominated by fossil fuel dependent power plants. Among the wealth of renewable energy sources, the non-concentrated photovoltaics witness the fastest growth (REN21, 2020). If the trends continue, photovoltaics will be the leading energy source in the 21st century.

Although the renewable energy relies on abundant and free energy sources, such as the Sun and wind, there are costs associated with operation and maintenance. In photovoltaics, despite the manufacturer's guarantee of linear power output degradation over time, long-term studies have shown the degradation rate is non-linear (Chattopadhyay et al., 2018; Sharma and Chandel, 2016) and significantly influenced by various environmental factors (Dubey et al., 2017). Thus, the loss of generated power equals the loss of revenue, which gives an incentive to prevent loss of generated power in a timely manner.

Therefore, precise understanding of the degradation in PV panels is an important milestone in maximizing the power yield and lifetime of PV plants. The latest trends in preventive maintenance use I–V characterization and electroluminescent (EL) imaging obtained by mobile test-beds. The tests are performed on-site at the level of individual PV panel.

The I–V characteristic *quantitatively* describes the *overall PV panel performance* by identifying explicit quantities such as: maximum power point P_{MPP}, short-circuit current I_{SC}, open-circuit voltage V_{OC} and derived quantities, such as fill-factor FF.

On the other hand, the EL image *qualitatively* documents *changes at the sub-cell level*. The most prominent information includes a crack formation (Spataru et al., 2018) and interconnect failures (Bosco et al., 2013; Jeong et al., 2012).

Correlation of these measurements by statistical models yields large variance in estimated power decline, since the severity of the fault is difficult to obtain from the EL image alone (Dubey et al., 2017; Kntges et al., 2011).

The state-of-the-art research on characterizing the performance of PV panels is based on establishing proper models with different granularity. The role of the model is to represent electrical characteristics of photovoltaic device(s), given the measurements or known external factors. A comprehensive list introducing an overview of modeling methods is depicted in Fig. 1, which classifies the work according to the level of granularity and intended application of the proposed model.

Photovoltaic devices are commonly connected in series to boost the overall voltage and lower the resistive losses due to large currents. Therefore, any mismatch among the devices, such as partial shading,
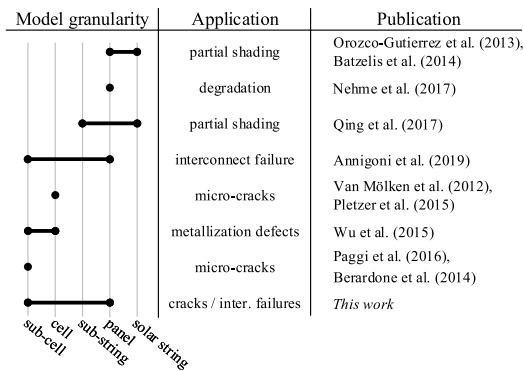

Fig. 1. Overview of state-of-the-art literature for modeling photovoltaic devices according to model granularity and application.

Fig. 2. Flowchart of the degradation identification method based on the proposed model formulated as a regression problem.

leads to sub-optimal operation of all serially connected devices. Although this publication addresses permanent degradation, partial shading establishes a general scenario for models representing mismatched solar generators connected in series.

The main focus of methods related to partial shading is often related to efficient model evaluation, such that the impact of partial shading is evaluated in real-time to assist power extracting algorithms. The work in Orozco-Gutierrez et al. (2013) models whole PV string and evaluates it by Newton–Raphson method, while in Batzelis et al. (2014) the same problem is solved by summing up voltages across serially connected PV panels based on Lambert function. The work of Qing et al. (2017) proposes conditional evaluation of by-pass diodes, which are evaluated only when conducting current. Models for partial shading neglect the sub-cell level granularity in order to achieve efficient evaluation.

On the other hand, models with sub-cell level granularity often reach the resolution of single bus-bar finger (Van Mölken et al., 2012; Pletzer et al., 2015; Paggi et al., 2016) investigating the degradation at microscopic level. While providing excellent insight into understanding of metallization defects (Wu et al., 2015) and cracks (Berardone et al., 2014), they are often unable to efficiently scale to the level of PV panel to reproduce the overall I–V characteristic.

In this regard, an ambitious model set to replicate long-term degradation of PV panel is introduced and experimentally verified in Nehme et al. (2017). The model is an equivalent double-diode model with bulk parameters expressed as functions of time. The bulk double-diode model parameters average over the degradation of individual solar cells, thus neglecting the cell and sub-cell level granularity.

The gap in sub-cell level and panel level granularity has been addressed in Annigoni et al. (2019), where detailed model of a PV panel with a sub-cell level resolution is presented and verified for interconnect failure detection from EL images. Although, the model yields excellent results, it rigidly simulates PV panel's overall I–V characteristic with interconnect failures only.

This article proposes a novel equivalent circuit model with variable modeling granularity. The granularity is based on sub-cell level analysis observed in an EL image. The model is able to reproduce I–V characteristics of the degraded PV panel cells with high accuracy, reflecting the sub-cell level degradation. The performance of the model and the evaluation algorithm are demonstrated on degradation identification task illustrated in Fig. 2.

The outcome of the identification task are the model parameters, which quantify the degradation at the sub-cell level.

Although there are multiple degradation modes that can occur in PV panels, the focus of this study are cracks and interconnect failures, because they are irreversible and cause hard-to-predict loss of generated power (Jordan et al., 2017).

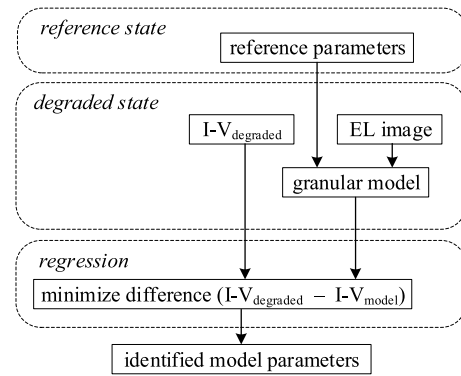In comparison to other models, the proposed model allows for detailed modeling of sub-cell level degradation compared to Nehme et al. (2017) and Annigoni et al. (2019), while generalizing the sub-cell level effects to the PV panel level as opposed to models in Wu et al. (2015) and Paggi et al. (2016).

The core contributions of this publication are:

- PV panel model in form of equivalent circuit model reproducing degraded I–V characteristic, taking into account sub-cell level degradation observed in EL image, such as cracks and interconnect failures.
- Formulation of a novel regression problem to determine parameters of degraded PV panel from measurements consisting of I–V characteristic and EL image.
- Verification of the proposed model and regression method on experimental measurements.

The structure of this publication is as follows:

Section 1 introduces the proposed equivalent circuit model with variable granularity. A double-diode model is introduced as a basic building block of the proposed model. The integration of degradation parameters based on geometrical criterion is explained. The steps to formulate the equivalent circuit model and the evaluation algorithm based on Newton–Raphson method are detailed.

Section 2 outlines the formulation of the regression problem. The formulation begins by definition of objective function to be minimized, continues by detailing the framework introduced by the model and concludes by an implementation of Evolutionary Algorithm based on Real Jumping-Gene Genetic Algorithm (RJGGA) to solve the regression problem.

Section 3 investigates the sensitivity of the model on external variables, such as the temperature and irradiation.

Section 4 verifies the proposed method on single cell and PV panel measurements.

Section 5 summarizes the results and concludes the publication.

1. Model of degraded PV panel

Solar cells are commonly modeled by equivalent circuit models, which incorporate one or more diodes to model non-linearity of I–V characteristic. A single-diode model assumes a combined effect of diffusion and recombination mechanisms while the double and multi-diode models distinguish these effects into constituent parts, achieving higher accuracy (Humada et al., 2016; Chen et al., 2018).

In this work, the double-diode model (Yahya-Khotbehsara and Shahhoseini, 2018) of Fig. 3 is adopted and enhanced by an extension component $I_{a-b(v)}$ to represent avalanche breakdown (Bishop, 1988) in the IV. quadrant of I–V characteristic.
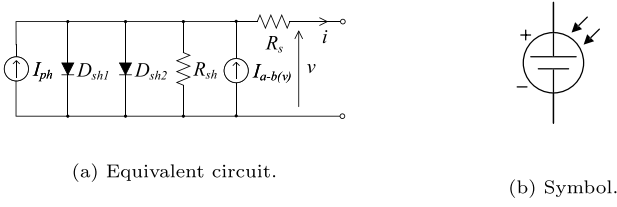
(a) Equivalent circuit.
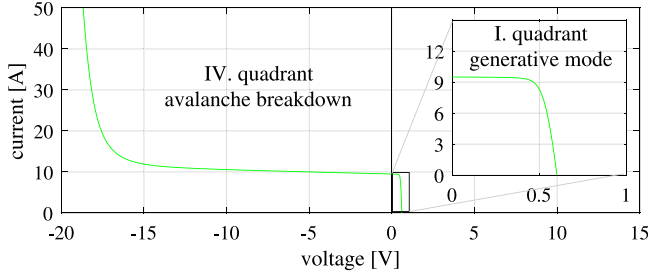
(b) Symbol.

Fig. 3. Double-diode model.

Fig. 4. Typical I–V characteristic of a solar cell described by Eq. (1).

The equivalent circuit in Fig. 3a is described by implicit equation

$$
\overbrace{i = I_{ph} - I_{01}\left(exp\left(\frac{v+iR_s}{V_{t1}}\right)-1\right) - I_{02}\left(exp\left(\frac{v+iR_s}{V_{t2}}\right)-1\right) - \frac{(v+iR_s)}{R_{ph}}}^{\text{double-diode model}}
$$
$$
\underbrace{- \frac{(v+iR_s)}{R_{ph}}\left[a\left(1-\frac{v+iR_s}{V_{br}}\right)^{-m}\right]}_{\text{avalanch breakdown}}.
$$

(1)

Evaluation of Eq. (1) across positive and negative voltage yields an I–V characteristic depicted in Fig. 4.

The double-diode model has been successfully used to describe photovoltaic devices with various granularity, from sub-cell level (Annigoni et al., 2019), cell level (Rossi et al., 2015) to approximating a PV panel (Nehme et al., 2017; Petrone et al., 2007). Although the granularity of the mathematical model covers wide range of photovoltaic devices, a set of parameters $\{I_{ph}, I_{01}, V_{t1}, I_{02}, V_{t2}, R_s, R_{sh}, V_{br}, a, m\}$ strictly represents a monolithic device.

Cracks introduce interfaces within the cell substrate, partitioning the cell into sub-parts, influencing the current flow through the solar cell. The interconnect failures impact the conductive pathways within the PV panel, causing uneven current flow through the affected solar cells. Cracks are usually caused by mechanical stress, such as hailstorm, strong winds or snow coverage, while the interconnect failures are caused by difference in thermal expansion coefficients of the silicon substrate and the metal interconnect, resulting in thermal stress. Although the interconnect failures introduce finite number of combinations, the cracks make the problem combinatorially intractable, since they exist in continuous domain. In another words, a cell can be cracked in limitless number of ways.

Therefore, the model is required to adapt to the observed degradation in EL image and reflect the affected sub-cell area and severity of the faults at the overall I–V characteristic.

1.1. Incorporation of degradation into the solar cell model

To accommodate cracks and interconnect failures that influence variable amount of cell area, the parameters of Eq. (1) are expressed as functions of parameters w [%], h [cell] and R_x [Ω] as outlined in Eq. (2). These expressions are similar to expressions derived in Bastidas et al.

(2013), where the equivalent of w and h is introduced at the cell-level, expressing parallel and serial connection of solar cells.

$$
\begin{aligned}
I_{ph(w,h)} &= \frac{w}{100} \times I_{ph,PV\ panel} \\
I_{01(w,h)} &= \frac{w}{100} \times I_{01,PV\ panel} \\
V_{t1(w,h)} &= \frac{h}{N_{cell}} \times V_{t1,PV\ panel} \\
I_{02(w,h)} &= \frac{w}{100} \times I_{02,PV\ panel} \\
V_{t2(w,h)} &= \frac{h}{N_{cell}} \times V_{t2,PV\ panel} \\
R_{s(w,h,R_x)} &= \frac{h}{N_{cell}}\frac{100}{w} \times R_{s,PV\ panel} + h \times R_x \\
R_{sh(w,h)} &= \frac{h}{N_{cell}}\frac{100}{w} \times R_{sh,PV\ panel} \\
V_{br(w,h)} &= \frac{h}{N_{cell}} \times V_{br,PV\ panel} \\
a &= a_{PV\ panel} \\
m &= m_{PV\ panel}
\end{aligned}
$$

(2)

The N_{cell} is the total number of solar cells in the PV panel.

In contrast to Bastidas et al. (2013), the parameter w represents the amount of cell's area at the sub-cell level. This reflects the inherent nature of crystalline solar cells as a parallel connection of sub-cell level elements connected by front and back metalization. Therefore, selecting the parameter $w \leq 100$ [%] represents whole or part of a solar cell's area.

The parameter h, similarly to Bastidas et al. (2013), is an integer representing number of solar cells connected in series. Selecting $h \geq 1$ represents 1 or more solar cells in series.

The parameter R_x represents severity of damage, which limits the flow of current.

1.2. Formulation of equivalent circuit model

The formulation of the proposed model as an equivalent circuit model is illustrated in Fig. 5 on a single sub-string of 18 solar cells in series with by-pass diode in parallel.

The formulation of the equivalent circuit model follows these steps:

Step 1 Identify degradation of solar cells from EL image and reorder the cells according to severity of the damage.

Step 2 Represent the degraded cells by the amount of affected area (quantify the amount of affected area by parameter w).

Step 3 Cluster the solar cells with similar degradation, such that a single large congregated cell ($h > 1$) averages degradation over multiple physical cells. The performance of sub-string (the conduction of by-pass diode) is influenced by the most damaged solar cell; therefore it is represented individually ($h = 1$).

Step 4 Represent the severity of degradation by resistance R_x. The parameters $\{I_{ph}, I_{01}, V_{t1}, I_{02}, V_{t2},$ $R_s, R_{sh}, V_{br}, a, m\}$ for sub-cell level components are obtained according to Eq. (2) using parameters $w_{[i,j]}$, $h_{[i]}$, $R_{x[i,j]}$. By-pass diode is included in parallel to serially connected elements.

The equivalent circuit model is further referred to as a function f_{model}, which is parametrized by a set $\{w_{[i,j]}, h_{[i]}, R_{x[i,j]}\}$. To simplify the model's nomenclature, the terms Super-cell and sub-cell are adopted throughout the rest of the text with the following meaning:

Super-cell S-$c_{[i]}$ refers to ith serially connected element within the equivalent circuit model. For instance, there are 4 Super-cells S-$c_{[1]}$ to S-$c_{[4]}$ in Fig. 5. The S-$c_{[4]}$ represents 9 physical solar cells without degradation. The S-$c_{[1]}$ represents single physical solar cell, parted into 3 sub-cells.

Sub-cells s-$c_{[i,j]}$ for $j = 1, \ldots, J$ represent J parallel parts of Super-cell S-$c_{[i]}$. Every sub-cell is a function s-$c_{[i,j]} = f(w_{[i,j]}, h_{[i]}, R_{x[i,j]})$, which represents the Eq. (1) with derived parameters $\{I_{ph(w,h)},$
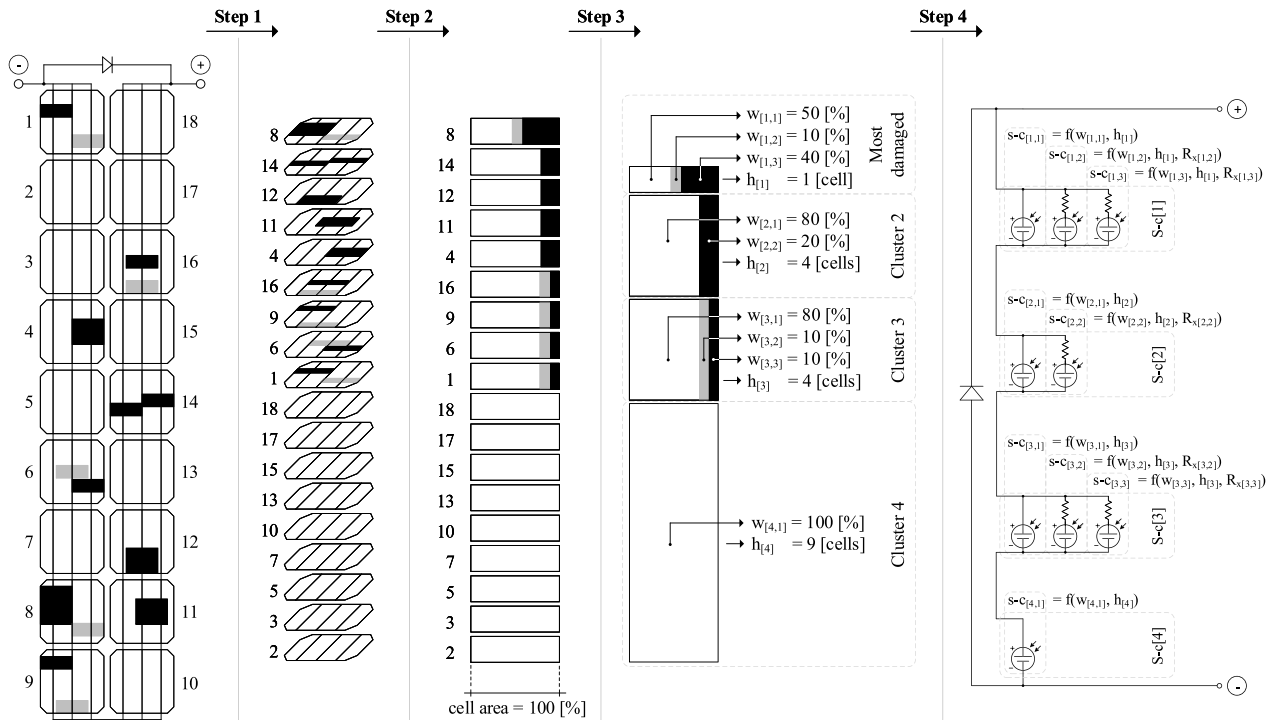
Fig. 5. Formulation of equivalent circuit model f_{model} in 4 steps based on EL image. The relation of parameters w and h is illustrated in Step 3. Step 4 introduces parameter R_x representing severity of degradation.
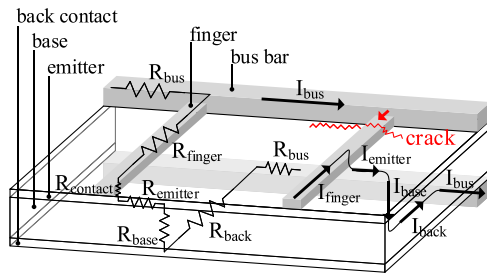

Fig. 6. Metallization resistances and current flow through cracked solar cell.

$I_{01(w,h)}$, $V_{t1(w,h)}$, $I_{02(w,h)}$, $V_{t2(w,h)}$, $R_{s(w,h,Rx)}$, $R_{sh(w,h)}$, $V_{br(h)}$, a, m}. For instance, the Super-cell $S\text{-}c_{[1]}$ in Fig. 5 consists of 3 sub-cells $s\text{-}c_{[1,1]}$, $s\text{-}c_{[1,2]}$ and $s\text{-}c_{[1,3]}$, representing areas with various levels of degradation.

1.3. Estimating the localized cell degradation from EL images

The current flow through a crystalline solar cell is formed by resistivity of the silicon substrate and metallization as illustrated in Fig. 6. In a reference state, the current is evenly distributed across the solar cell.

A crack or interconnect failure causes a change in current pathways. An example in Fig. 6 depicts a crack preventing current flow from the bus-bar. The current I_{finger} of the affected finger needs to travel longer distance from neighboring bus-bar (not depicted). The cumulative resistance R_{finger} lowers the amount of current that reaches the substrate near the crack. Consequently, the current density is lower in the affected region, which is observed in EL image as area with lower emission of near-infrared light.

The amount of area affected by cracks is studied in Paggi et al. (2014), where a geometrical criterion is proposed. The criterion states
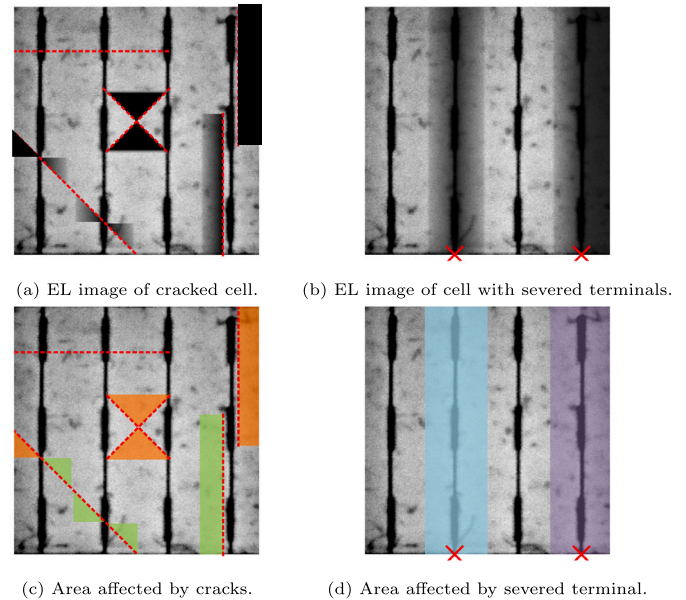

(a) EL image of cracked cell.

(b) EL image of cell with severed terminals.

(c) Area affected by cracks.

(d) Area affected by severed terminal.

Fig. 7. Application of geometrical criterion. (For interpretation of the references to color in this figure legend, the reader is referred to the web version of this article.)

that the amount of affected area is determined by the direction and position of the crack.

We extend the geometrical criterion to the case of severed interconnect bus-bar(s), which stems from findings in Annigoni et al. (2019). The geometrical criterion and its application on EL image is illustrated in Fig. 7.

The red dashed lines in Fig. 7 represent cracks. The full red crosses represent severed interconnect bus-bars. The areas with gradient or

black in color, in Figs. 7a and 7b, illustrate lower intensity of emitted near-infrared light.

The color-coded areas depicted in Figs. 7c and 7d marks the expected area being affected according to geometrical criterion. Parameter w_{expect} [%] represents the percentage of affected area.

Since the impact of cracks is distinguishable according to the direction and position and also differs from the impact of severed bus-bars, the categorization to mild (illustrate by green, blue & purple color) and severe (orange color) fault is adopted. Mild degradation causes increased resistance, due to prolonging the pathways the current needs to traverse. Therefore, mild degradation is related to parameter R_x and w_{expect}. Severe degradation prevents the current flow through the affected area. This lowers the total amount of current the solar cell can sustain in generative mode, thus lowering the short circuit current I_{SC}. Therefore, severe degradation lowers the total area, such that $w_{active} = w_{solar\ cell} - w_{expect}$ or in terms of model parameters $\sum_j w_{[i,j]} < 100$ [%].

In reality, it is reasonable to expect intermediate interfaces where cracks may partially conduct. Therefore, the EL image is used to decide the structure and granularity of the proposed model, while the parameter values are obtained by regression. The requirement on the quality of the EL image is such, that it sufficiently distinguishes the major cracks and the regions of cells affected by the interconnection failures, which is the usual case of EL imaging performed for industrial diagnostics in the field.

1.4. Efficient evaluation of f_{model}

A fast and precise evaluation algorithm enables to deploy the model in tasks that are independent of commercial simulation tools. In this case, a standalone evaluation algorithm is introduced, which is necessary for solving regression in Section 2.

Firstly, we explain the iterative solver based on Newton–Raphson algorithm proposed to solve the voltage $V = \{v_1, \ldots, v_n, \ldots, v_N\}$ based on current vector $I = \{i_1, \ldots, i_n, \ldots, i_N\}$ through a single Super-cell. For this purpose, we re-introduce the f_{model} from Fig. 5 in greater detail in Fig. 8, depicting the Kirchoff's law voltage loops L_1, L_2 and the current preservation node N_1 for Super-cell S-$c_{[1]}$.

The subscript [1] of the Super-cell S-$c_{[1]}$ is dropped in to simplify the notation. Furthermore, since the algorithm is iterative, we denote the Newton–Raphson's iteration by subscript (t). The algorithm starts with Kirchhoff's voltage and current laws yielding the following vector function **F**,

$$\mathbf{F} = \begin{bmatrix} f_{L_1} \\ f_{L_2} \\ f_{N_1} \end{bmatrix} = \begin{bmatrix} -v_{[1](t)} + v_{[2](t)} \\ -v_{[1](t)} + v_{[3](t)} \\ -i_{[1](t)} - i_{[2](t)} - i_{[3](t)} + i_n \end{bmatrix}. \tag{3}$$

The Jacobian matrix is derived in order to perform Newton–Raphson update

$$J = \begin{bmatrix} \frac{\partial f_{L_1}}{\partial v_{[1]}} & \frac{\partial f_{L_1}}{\partial v_{[2]}} & \frac{\partial f_{L_1}}{\partial v_{[3]}} \\ \frac{\partial f_{L_2}}{\partial v_{[1]}} & \frac{\partial f_{L_2}}{\partial v_{[2]}} & \frac{\partial f_{L_2}}{\partial v_{[3]}} \\ \frac{\partial f_{N_1}}{\partial v_{[1]}} & \frac{\partial f_{N_1}}{\partial v_{[2]}} & \frac{\partial f_{N_1}}{\partial v_{[3]}} \end{bmatrix} = \begin{bmatrix} -1 & -1 & 0 \\ -1 & 0 & -1 \\ -\frac{\partial i_{[1]}}{\partial v_{[1]}}\Big|_{(t)} & \frac{\partial i_{[2]}}{\partial v_{[2]}}\Big|_{(t)} & \frac{\partial i_{[3]}}{\partial v_{[3]}}\Big|_{(t)} \end{bmatrix}. \tag{4}$$

The last row of Jacobian matrix J requires evaluation of derivative of implicit function. Implicit Function Theorem states that

$$\frac{\partial i(v)}{\partial v} = -\frac{\frac{\partial f(v,i)}{\partial v}}{\frac{\partial f(v,i)}{\partial i}}. \tag{5}$$

The evaluation of Eq. (5), where $f_{(v,i)} = 0$ is obtained by moving left-hand side of Eq. (1) to right-hand side, is as follows:
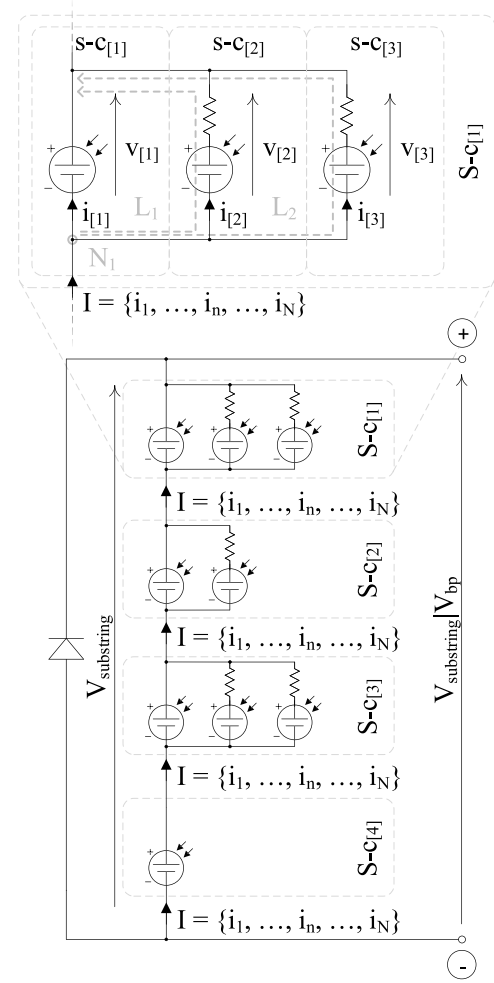

Fig. 8. Illustration of substring evaluation with Kirchhoff laws marked down for Super-cell S-$c_{[1]}$ consisting of three sub-cells. The quantities $V_{substring}$, $V_{substring}|V_{bp}$ and I are marked down as visual guidance for the reader to relate the voltages and currents inside the model to the evaluation process illustrated in Fig. 9.

1. Partial differentiation of $f_{(v,i)}$ according to v:

$$\begin{aligned} \frac{\partial f_{(v,i)}}{\partial v} = &-\frac{I_{01}}{V_{t1}} exp\left(\frac{v + iR_s}{V_{t1}}\right) - \frac{1}{R_{sh}} \\ &- \frac{I_{02}}{V_{t2}} exp\left(\frac{v + iR_s}{V_{t2}}\right) \\ &- \frac{a}{R_{sh}}\left(1 - \frac{v + iR_s}{V_{br}}\right)^{-m}\left(1 - \frac{m(v + iR_s)}{v + iR_s - V_{br}}\right). \end{aligned} \tag{6}$$

2. Partial differentiation of $f_{(v,i)}$ according to i:

$$\begin{aligned} \frac{\partial f_{(v,i)}}{\partial i} = &-\frac{I_{01}R_s}{V_{t1}} exp\left(\frac{v + iR_s}{V_{t1}}\right) - \frac{R_s}{R_{sh}} - 1 \\ &- \frac{I_{02}R_s}{V_{t2}} exp\left(\frac{v + iR_s}{V_{t2}}\right) \\ &- \frac{aR_s}{R_{sh}}\left(1 - \frac{v + iR_s}{V_{br}}\right)^{-m}\left(1 - \frac{m(v + iR_s)}{v + iR_s - V_{br}}\right). \end{aligned} \tag{7}$$

It is easy to see then that $\frac{\partial f_{(v,i)}}{\partial i} = \frac{\partial f_{(v,i)}}{\partial v} Rs - 1$. Therefore, if $\beta = \frac{\partial f_{(v,i)}}{\partial v}$, the derivative in Jacobian is

$$\frac{\partial i(v)}{\partial v} = \frac{1}{\frac{1}{\beta} - R_s}. \tag{8}$$
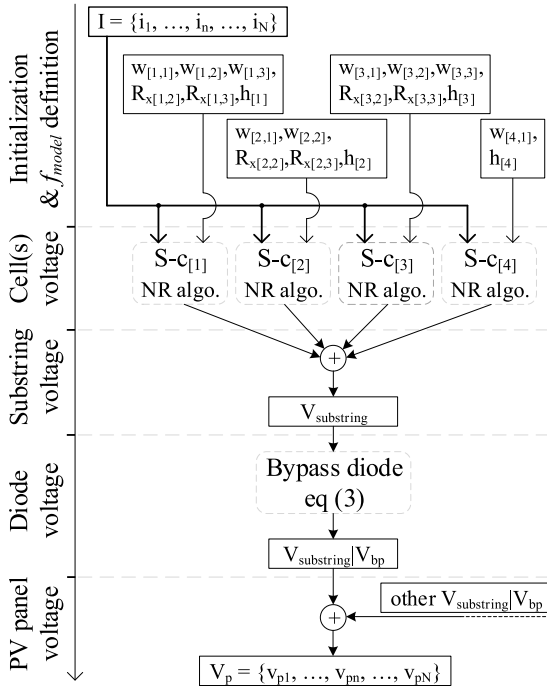
Fig. 9. Illustration of the f_{model} evaluation algorithm from computational perspective. Operations stacked vertically are necessarily performed sequentially. Operations placed vertically next to each other are mutually independent, thus utilizing the potential of parallel execution.

The Newton–Raphson update for the dependent variable $\mathbf{v} = [v_{[1](t)}, v_{[2](t)}, v_{[2](t)}]^T$ at iteration (t) is

$$\mathbf{v}_{(t)} = \mathbf{v}_{(t-1)} - J^{-1}\mathbf{F}. \tag{9}$$

The Eq. (9) is iteratively solved until the error $\epsilon = \|\mathbf{F}\| < 10^{-10}$ for every sample $i_n \in I$.

Secondly, for the by-pass diode component in Fig. 8 we adopt a similar evaluation method as proposed by Qing et al. (2017), who recognized that the by-pass diode installed in parallel to PV cells conducts current only when the voltage across the by-pass diode $V_{bp} \leq V_{substring}$, where the common limit for a by-pass diode to conduct is ≈ -0.7 [V], thus the condition for conduction is $V_{substring} \leq -0.7$ [V]. The vector $V_{substring}|V_{bp}$ denoting the vector $V_{substring}$ including the effect of conditional by-pass diode conduction is evaluated as follows

$$V_{substring}|V_{bp} = \begin{cases} -V_{bp} \times ln\left(\frac{I-I_{SC}}{I_0^{bp}}+1\right), & \text{if } V_{substring} \leq -0.7 \text{ [V]} \\ V_{substring}, & \text{otherwise.} \end{cases} \tag{10}$$

Lastly, we propose a motivation to choose vector I as an independent variable and $V_{Super-cell}$, thus $V_{substring}$ and V_{panel} as a dependent variable. The motivation stems from the work of Batzelis et al. (2014), who in a similarly complex problem related to partially-shaded PV array concluded that:

- a summation operation of vectors has negligible computational cost
- the computational cost of Newton–Raphson method is proportional to the size of Jacobian Matrix J

Therefore, preferring vector summation, rather than the evaluation of large system of equations, we propose the computational perspective on evaluating the f_{model} illustrated in Fig. 9.

The computational procedure is as follows:

1. Define the f_{model} according to steps outlined in Section 1.2 and initialize the discretized vector $I = \{i_1, \dots, i_N\}$ with N samples.
2. Evaluate the voltage vectors $V_{Super-cell}$. Every instance of Super-cell $S\text{-}c_{[i]}$ can be evaluated as an independent problem.
3. Perform vector summation $V_{substring} = \sum_i V_{Super-cell,i}$, since the voltage vectors are defined over the same current vector I. The vectors $V_{Super-cell,i}$ represent Super-cells, thus physical PV cells, connected in series.
4. Conditionally apply Eq. (10) to the samples of vector $V_{substring}$.
5. Perform vector summation on $V_{substring}|V_{bp}$, if the PV panel includes more substrings in series. The same reasoning from the *point 3.* applies.

In summary, by keeping the $V_{substring}$ and $V_{substring}|V_{bp}$ outside of the Newton–Raphson algorithm, the Jacobian matrix J describes the minimum number of elements. These elements are sub-cells $s\text{-}c_{[i,j]}$, thus the dimension of Jacobian matrix is $j \times j$, the smallest possible for this kind of model. The rest of the evaluation algorithm consists of vector summations and conditional evaluation of Eq. (10), which have negligible computational costs.

2. Regression of equivalent circuit model f_{model} to degraded I–V characteristic

A flowchart of the proposed regression method is depicted in Fig. 10.

Following Fig. 10, the regression method begins by characterizing the *reference state* of the PV panel by double-diode model parameters $\{I_{ph}, I_{01}, V_{t1}, I_{02}, V_{t2}, R_s, R_{sh}, V_{br}, a, m\}$. These parameters are obtained from datasheet values (Cannizzaro et al., 2014) or reference I–V characteristic (Macabebe et al., 2011; Gong and Cai, 2013).

The *degraded state* is documented by measured degrade I–V characteristic and EL image. The analysis of EL image, based on geometrical criterion explained in Section 1.3, yields the expected affected area w_{expect} and severity of degradation for every degraded cell within the PV panel. These parameters are used to formulate the model f_{model} following the 4 steps outlined in Section 1.2. The equivalent circuit model f_{model} then provides a framework for representing the degradation as a state of sub-cells $s\text{-}c_{[i,j]}$ characterized by a set of parameters $w_{[i,j]}$, $h_{[i]}$ and $R_{x[i,j]}$.

The *regression* solves a minimization problem for a subset of these parameters, referred to as optimization vector θ. Usually $\{w_{[i,j]}, R_{x[i,j]}\} \in \theta$, since the number of solar cells $h_{[i]}$ is easily determined from the EL image.

The objective function $f_{obj,V}(\theta)$ is a measure of error between the measured degraded I–V characteristic and the I–V characteristic obtained by evaluating f_{model}. Since the current vector I is given, as explained in Section 1.4, the objective function is formulated as an ℓ^2-norm of the difference of voltage vectors:

$$f_{obj,V}(\theta) = \left\| V_{degrad}|_I - V_{model}(\theta, I) \right\|, \tag{11}$$

where $V_{model}(\theta, I)$ is obtained by evaluating f_{model} for a set of parameters θ and current vector I. The $V_{degrad}|_I$ denotes the translation of the measured degraded I–V characteristic into a voltage vector V_{degrad} given the current vector I.

The regression problem is formally stated as:

$$\arg\min_{\theta} f_{obj,V}(\theta). \tag{12}$$

The minimization of Eq. (12) over the optimization vector θ is solved by Evolutionary Algorithm.

2.1. Regression by evolutionary algorithm

Evolutionary Algorithms are general purpose optimization algorithms with robust performance irrespective of initial conditions and
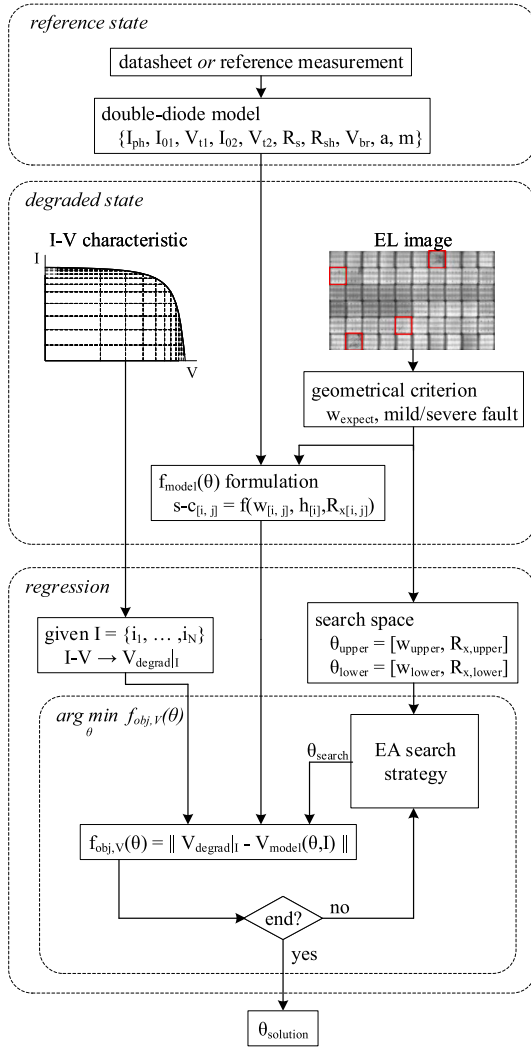
Fig. 10. Information flow of the proposed regression method.

Fig. 11. Iterative principle of RJGGA.

- For mild degradation $R_{x,upper[i,j]} = 0 \leq R_{x[i,j]} \leq R_{x,mild}^{limit} = R_{x,lower[i,j]}$.
- For severe degradation $R_{x,upper[i,j]} = R_{x,mild}^{limit} < R_{x[i,j]} \leq R_{x,severe}^{limit} = R_{x,lower[i,j]}$.

It should be noted that the search limits for mild and severe degradation are mutually exclusive, such that $0 \leq R_{x,mild} \leq R_{x,mild}^{limit} \leq R_{x,severe} \leq R_{x,severe}^{limit}$, which assures the EA does not misinterpret the observed severity of the degradation during the optimization.

2.2. Iterative search strategy of RJGGA

The evolutionary search strategy of Real Jumping-Gene Genetic Algorithm (RJGGA) is adopted, which performs well on similarly complex objective function for identification of dynamic diode-model parameters, which we implemented in Garaj et al. (2020).

The implementation of RJGGA is illustrated in Fig. 11.

The evolution of solutions θ_{search} begins from random initialization of K vectors $\theta_{search,k}$, where $k = 1, \ldots, K$, such that $\theta_{search,k} \in (\theta_{lower}, \theta_{upper}) \, \forall \, k$. Each $\theta_{search,k}$ is evaluated for value $f_{obj,V}$, such that it forms a tuple $\langle \theta_{search}, \, f_{obj,V}(\theta_{search}) \rangle$.

The parent selection selects P parent tuples, such that $P < K$ (usually $P \ll K$), with low value of $f_{obj,V}$. The according $\theta_{search,p}$, where $p = 1, \ldots, P$, are used to generate set of K new $\theta_{search,k}$ using jumping, crossover and mutation operations. At the end, the newly generated $\theta_{search,k}$ are evaluated for value $f_{obj,V}$, closing the loop.

The iterations continue until the convergence criteria, which is fulfilled when reaching predefined number of iterations. After convergence condition, the θ_{search} attaining the lowest value of $f_{obj,V}$ represents the parameters of f_{model}, which best describes the electrical changes in the measured degraded I–V characteristic according to observations in EL image.

3. Sensitivity analysis

This section illustrates the sensitivity of the proposed model to the internal and external parameters. The deviations in these parameters

---

not relying on gradient information, significantly simplifying the problem formulation. As such, EAs have long standing record in photovoltaics (Macabebe et al., 2011; Ishaque et al., 2012; Gong and Cai, 2013; Dkhichi et al., 2014; Singh et al., 2015) when performing regression on problems similar to Eq. (12).

On the other hand, EAs require prior knowledge of bounded search space $\{\theta_{lower}, \theta_{upper}\}$, within which the final solution $\theta_{solution}$ is searched. This need for prior knowledge often limits the use of EAs, since many problems require to discover the solution irrespective of bounds. The proposed regression method uses the requirement of prior knowledge to its advantage, since the constraints on θ are naturally derived from the EL image.

The search limits $w_{lower} \in \theta_{lower}$ and $w_{upper} \in \theta_{upper}$ are determined based on w_{expect} as follows:

- For mild degradation, the $w_{lower[i,j]} = w_{expect[i,j]} - \eta \leq w_{[i,j]} \leq w_{expect[i,j]} + \eta = w_{upper[i,j]}$.
- For severe degradation $w_{lower[i,j]} = 0 \leq w_{[i,j]} \leq w_{expect[i,j]} + \eta = w_{upper[i,j]}$.

The parameter η represents uncertainty related to application of the geometrical criterion.

The search limits $R_{x,lower} \in \theta_{lower}$ and $R_{x,upper} \in \theta_{upper}$ are determined as follows:
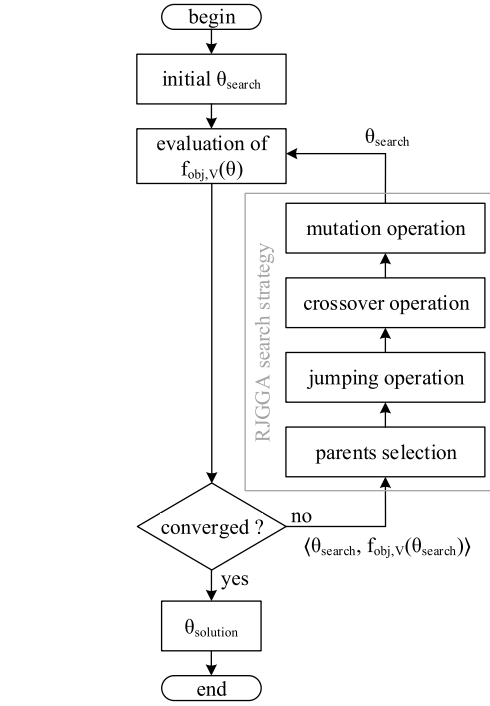
Table 1
Reference double-diode model parameters for a single solar cell.

$I_{ph,ref}$ [A]	$I_{01,ref}$ [A]	$V_{t1,ref}$ [V]	$I_{02,ref}$ [A]	$V_{t2,ref}$ [V]	$R_{s,ref}$ [Ω]	$R_{sh,ref}$ [Ω]
8.617	6.116^{-10}	0.028	7.625^{-11}	0.0565	0.010	120

Table 2
Temperature and irradiance coefficients for Eqs. (13).

$k_{I_{ph}}$ [%/°C]	k_{R_s} [%/°C]	$k_{R_{sh}}$ [%/°C]	γ_{R_s} [–]	$\gamma_{R_{sh}}$ [–]
0.2	2.5	−1.0	−0.7	−1.5

cause a measurable error, which is used by the RJGGA to navigate the parameter space during the regression. Both, the internal model parameters, w and R_x, and the external parameters, temperature T and irradiation G, are investigated.

The effect of T and G is incorporated into the proposed model through the double-diode parameters (Silva et al., 2017)

$$I_{ph(T,G)} = \left[I_{ph,ref} + k_{I_{ph}} (T - T_{ref}) \right] \frac{G}{G_{ref}}$$

$$I_{01(T,G)} = I_{01,ref} \left(\frac{T}{T_{ref}} \right)^3 exp \left[\frac{qE_g}{kn} \left(\frac{1}{T} - \frac{1}{T_{ref}} \right) \right]$$

$$V_{t1(T,G)} = V_{t1,ref} \left(\frac{T}{T_{ref}} \right)$$

$$I_{02(T,G)} = I_{02,ref} \left(\frac{T}{T_{ref}} \right)^3 exp \left[\frac{qE_g}{kn_2} \left(\frac{1}{T} - \frac{1}{T_{ref}} \right) \right] \qquad (13)$$

$$V_{t2(T,G)} = V_{t2,ref} \left(\frac{T}{T_{ref}} \right)$$

$$R_{s(T,G)} = R_{s,ref1} \left[1 + k_{R_s} (T - T_{ref}) \right] + R_{s,ref2} \left(\frac{G}{G_{ref}} \right)^{\gamma_{R_s}}$$

$$R_{sh(T,G)} = R_{sh,ref} \left[1 + k_{R_{sh}} (T - T_{ref}) \right] \left(\frac{G}{G_{ref}} \right)^{\gamma_{R_{sh}}}.$$

The reference values of G and T are STC values, such that T_{ref} is 25 [°C], thus $T_{ref} = 298.15$ [K] and irradiation $G_{ref} = 1000$ [$\frac{W}{m^2}$]. The parameters q, k and E_g represent Boltzmann constant, electron charge and bandgap energy of silicon, respectively. Furthermore, according to Silva et al. (2017) the $R_{s1,ref} = R_{s2,ref} = R_{s,ref}/2$ and the diode ideality factor $n = \frac{V_t q}{kT}$.

Throughout this section we use the double-diode parameters at STC tabulated in Table 1.

The coefficient values characterizing the dependency on temperature T and irradiation G in Eqs. (13) are tabulated in Table 2.

The sensitivity analysis is performed as a parameter sweep within ranges:

- −5 [°C] ≤ T ≤ 55 [°C]
- 976 [$\frac{W}{m^2}$] ≤ G ≤ 1024 [$\frac{W}{m^2}$]
- 0.000 [Ω] ≤ R_x ≤ 0.060 [Ω]
- 0.0 [%] ≤ w_x ≤ 4.8 [%]

The quantification of the deviation by the function $f_{obj,V}(\theta)$ defined in Eq. (11) yields a magnitude of the error of mismatching I–V characteristics. For the purpose of this investigation, the $V_{degrad}|_I$ is replaced by $V_{init}|_I$, which describes the initial state of the simulated PV panel.

3.1. Case 1: single solar cell within a PV panel

The sensitivity in parameters T, G, w and R_x deviating within a single solar cell installed in a 60-cell PV panel is investigated. The f_{model} of the simulated PV panel is depicted in Fig. 12.

The parameters of the Super-cells $S\text{-}c_{[1-4]}$ and the corresponding sub-cells are tabulated in Table 3, the parameters in **bold** are used in the parameter sweep.
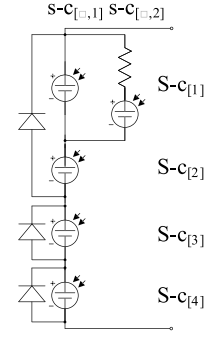
Fig. 12. Equivalent circuit model f_{model} for sensitivity analysis of a single solar cell.

Table 3
Parameters of the equivalent circuit model f_{model} in Fig. 12.

		w [%]	R_x [Ω]	h [cell]
$S\text{-}c_{[1]}(T_{[1]}, G_{[1]})$	$s\text{-}c_{[1,1]}$	75.00	–	1
	$s\text{-}c_{[1,2]}$	$25.0 - w_{x[1]}$	$R_{x[1]}$	
$S\text{-}c_{[2]}(T, G)$	$s\text{-}c_{[2,1]}$	100.0	–	19
$S\text{-}c_{[3]}(T, G)$	$s\text{-}c_{[3,1]}$	100.0	–	20
$S\text{-}c_{[4]}(T, G)$	$s\text{-}c_{[4,1]}$	100.0	–	20

Table 4
Parameters of the equivalent circuit model f_{model} in Fig. 14.

		w [%]	R_x [Ω]	h [cell]
$S\text{-}c_{[1]}(T_{[1]}, G_{[1]})$	$s\text{-}c_{[1,1]}$	75.00	–	1
	$s\text{-}c_{[1,2]}$	$25.00 - w_{x[1]}$	$R_{x[1]}$	
$S\text{-}c_{[2]}(T, G)$	$s\text{-}c_{[2,1]}$	100.0	–	19
$S\text{-}c_{[3]}(T_{[3]}, G_{[3]})$	$s\text{-}c_{[3,1]}$	75.00	–	1
	$s\text{-}c_{[3,2]}$	$25.00 - w_{x[3]}$	$R_{x[3]}$	
$S\text{-}c_{[4]}(T, G)$	$s\text{-}c_{[4,1]}$	100.0	–	19
$S\text{-}c_{[5]}(T, G)$	$s\text{-}c_{[5,1]}$	100.0	–	20

The initial values, representing the ground truth, are selected as $T_{[1]} = 25$ [°C], $G_{[1]} = 1000$ [$\frac{W}{m^2}$], $R_{x[1]} = 0.030$ [Ω] and $w_{x[1]} = 2.4$ [%].

The topology of the error surfaces depicted in Fig. 13 is the result of the sensitivity analysis performed on combinations of paired parameters $T_{[1]}$, $G_{[1]}$, $R_{x[1]}$ and $w_{x[1]}$. The global minimum is clearly distinguished despite the existence of multiple local minimums. Further, the global minimum is recovered even for cases of highly correlated variables, such as G and w (midpoint of bottom row within Fig. 13), which are primarily correlated through the double-diode parameter I_{ph}. The I_{ph} parameter shares the scaling factor $\frac{G}{G_{ref}}$ and $\frac{w}{100}$, respectively, as seen in Eqs. (2) and (13).

3.2. Case 2: two solar cells within a PV panel

We investigate the sensitivity of parameters within two solar cells, installed inside two different sub-strings of a 60-cell PV panel. The f_{model} of the simulated PV panel is depicted in Fig. 14.

The parameters of Super-cells $S\text{-}c_{[1-5]}$ and the corresponding sub-cells are tabulated in Table 4, the parameters in **bold** are used in the parameter sweep.

The initial values, representing the ground truth, are selected as $T_{[1]} = T_{[3]} = 25$ [°C], $G_{[1]} = G_{[3]} = 1000$ [$\frac{W}{m^2}$], $R_{x[1]} = 0.015$ [Ω], $w_{x[1]} = 3.6$ [%], $R_{x[3]} = 0.040$ [Ω] and $w_{x[3]} = 1.6$ [%].

The sensitivity analysis performed on the permutations of paired parameters T, G, R_x, w_x for sub-cells $s\text{-}c_{[1]}$ and $s\text{-}c_{[3]}$ is shown in Fig. 15.

The topology of the error surfaces depicted in Fig. 15 differ from those in Fig. 13, since the two solar cells are installed in two different sub-strings, the deviations are not correlated.
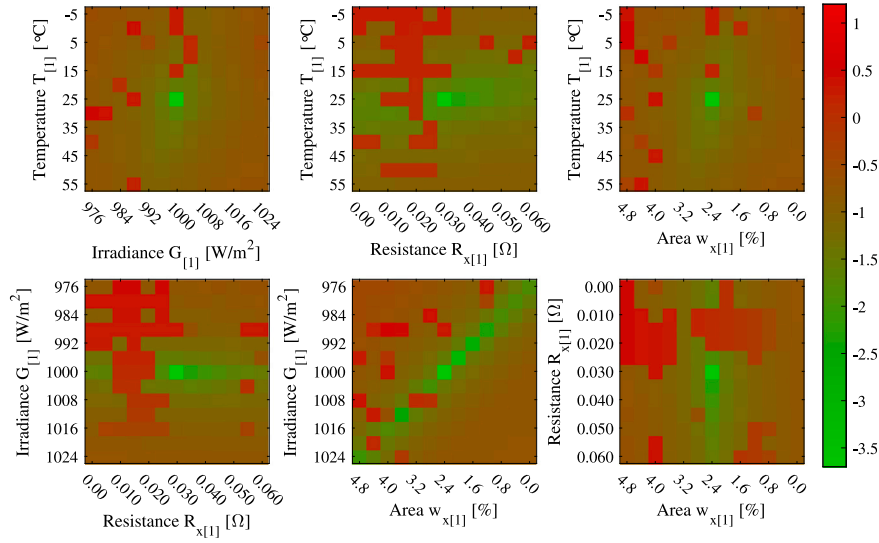
Fig. 13. Error value caused by T, G, R_x and w parameter deviations of a single solar cell inside a 60-cell PV panel.
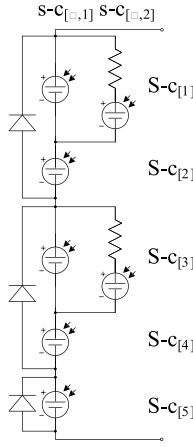

Fig. 14. Equivalent circuit model f_{model} for sensitivity analysis of two solar cells.

3.3. Findings from the sensitivity analysis

The topology of the error surfaces depicted in Figs. 13 and 15 show a block-like structure with regions of large error values. The sudden changes in the error surfaces are attributed to the sampling steps of T, G, R_x and w and the finite sampling of the vector I used in $f_{obj,V}(\theta)$.

The y-axis in Fig. 13 depicting the dependency on temperature T (upper row) hint a potential benefit of including Infra-Red imaging, in the case of the temperature deviation among individual cells greater than 10 [°C]. In such case, the error value $log_{10}(f_{obj,V}(\theta))$ is approximately one decade greater compared to the situation where the cell's temperature is known. Furthermore, according to Fig. 15, a deviation of more than 15 [°C] is responsible for introducing multiple local minimums within the error surface. This further motivates the use of non-convex solver during the regression, such as the RJGGA, which is capable of locating global minimum despite the existence of local minimums.

4. Experimental verification

The proposed model and the regression method is experimentally verified. Firstly, a set of destructive tests is performed on a set of stand-alone solar cells in controlled conditions. The tests verify the geometrical criterion extended to interconnect failures and the models ability to replicate effects of the observed degradation.

Secondly, a set of crystalline PV panels with cracks and interconnect failures are tested. The tested samples cover panels of various age and degradation. The tests are focused on generalization property of combining multiple similarly degraded cells into Super-cells.

4.1. Single solar cell verification

Three destructive tests are performed to study solar cell cracks and interconnect failures. The tested cells are 4.2 [W] poly-crystalline cells with 4 interconnect bus-bars. The testing is performed at Standard Testing Conditions (STC) at temperature 25 [°C] and irradiation 1000 [$\frac{W}{m^2}$] with a test-bed accommodating a single solar cell. The tests are distinguished according to the crack direction relative to the bus-bars: parallel, diagonal and perpendicular. Further, the tests include a severed bus-bar and the combination of severed bus-bar and cracks to simulate complex degradation.

The search limits $\{\theta_{lower}, \theta_{upper}\}$ are derived from color-coded Figs. 17a, 18a and 19a by geometrical criterion and are set as follows:

Green color-coded area refers to *mild* degradation, such that $0 [\Omega] \leq R_{x[2]} \leq 0.1 [\Omega]$ and $w_{[1]} = w_{expect,green} \pm 5 [\%]$.

Blue color-coded area signifies *potentially severe* degradation, thus $0.1 [\Omega] \leq R_{x[3]} \leq 10 [\Omega]$ and $w_{[3]} = w_{expect,blue} \pm 5 [\%]$.

Red color-coded area marks *severe* degradation, such that the flow of the current is halted, thus $R_{x[4]} = \infty [\Omega]$ and $0 [\%] \leq w_{[4]} \leq w_{expect,red} [\%]$. This means the parameter $w_{[4]}$ represents the amount of inactive area, thus the s-c$_{[4]}$ is not implemented as separate sub-cell, but simply as a smaller sub-cell s-c$_{[1]}$ area represented by $w_{[1]}$.

The I–V characteristics plotted in Figs. 17b, 18b and 19b show: reference, measured, model-predicted and worst case I–V characteristics. The worst case I–V characteristic is obtained by f_{model} given the observed area w_{expect} and parameters $\theta = \theta_{lower}$.

The regression is performed on parameters $\theta = \{w_{[i,j]}, R_{x[i,j]}\}$ that are highlighted in **bold** within Tables 5–7. The rest of the parameters are kept constant.

The equivalent circuit model f_{model} used in regression is depicted in Fig. 16.

The RJGGA parameters K, P and number of iterations until convergence are set to 50, 20 and 100 respectively.
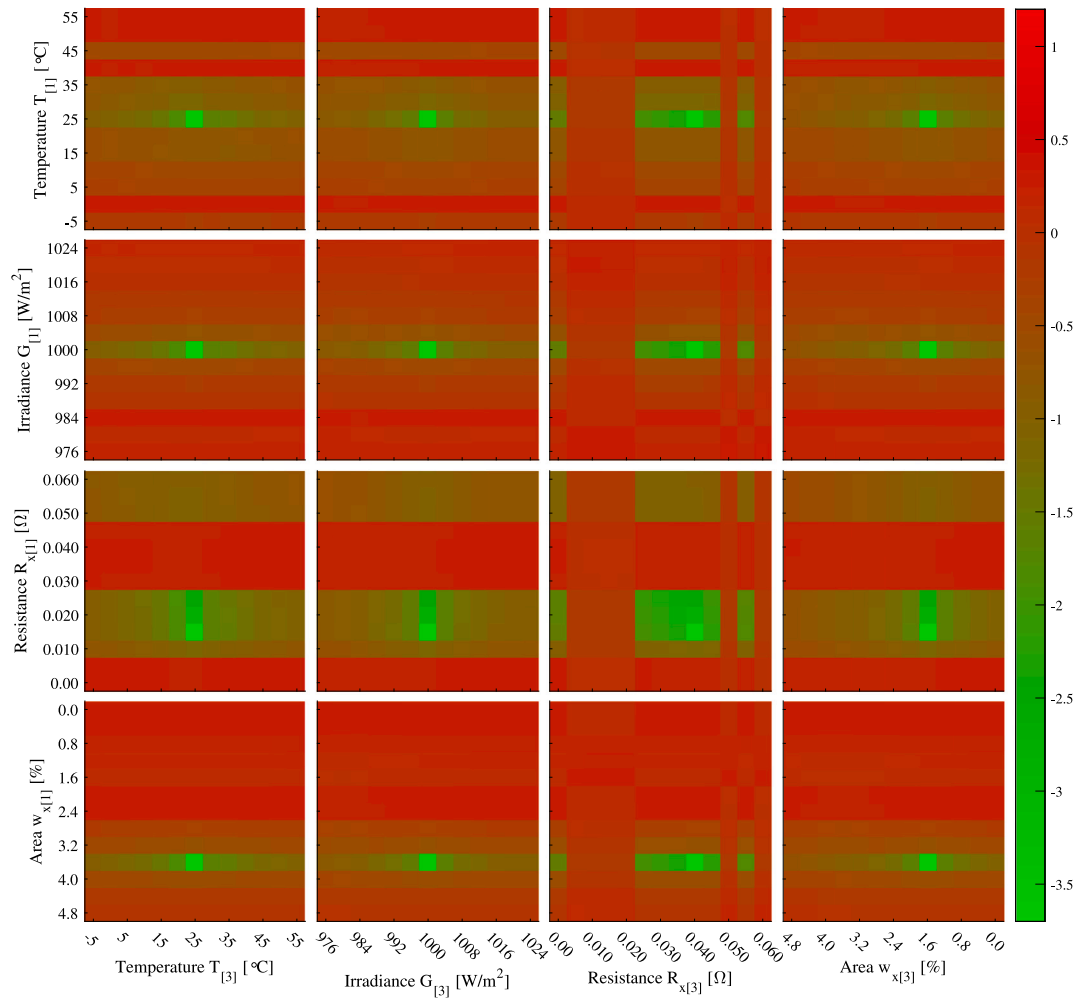
Fig. 15. Error values caused by T, G, R_x and w parameter deviations within two different solar cells of a 60-cell PV panel.
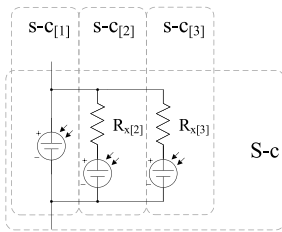

Fig. 16. Equivalent circuit model f_{model} for single cell measurements.

4.1.1. Case 1: parallel crack

A crack parallel to the bus-bars is investigated. Fig. 17 depicts taken EL images and the measured I–V characteristics.

Parameters identified by regression are tabulated in Table 5.

4.1.2. Case 2: diagonal crack

A crack diagonal to the bus-bars is investigated. Fig. 18 depicts taken EL images and the measured I–V characteristics.

Parameters identified by regression are tabulated in Table 6.

4.1.3. Case 3: lateral crack

A crack perpendicular to the bus-bars is investigated. Fig. 19 depicts taken EL images and the measured I–V characteristics.

Parameters identified by regression are tabulated in Table 7.

Table 5
Parameters of the equivalent circuit model f_{model} for single cell with parallel crack.

		w [%]	R_x [Ω]	w_{expect} [%]
S-c$_{(1a)}$	s-c$_{[1]}$	75.00	–	75.00
	s-c$_{[2]}$	25.00	0.020	25.00
S-c$_{(1b)}$	s-c$_{[1]}$	89.00	–	90.10
	s-c$_{[2]}$	4.20	0.030	4.40
	s-c$_{[3]}$	3.00	0.353	2.10
	–	3.80	–	3.30
S-c$_{(1c)}$	s-c$_{[1]}$	64.50	–	65.20
	s-c$_{[2]}$	29.60	0.018	29.30
	s-c$_{[3]}$	2.60	0.100	2.10
	–	3.80	–	3.30
S-c$_{(1d)}$	s-c$_{[1]}$	71.10	–	71.00
	s-c$_{[2]}$	17.90	0.050	18.40
	s-c$_{[3]}$	5.50	0.298	4.90
	–	5.50	–	5.70
S-c$_{(1e)}$	s-c$_{[1]}$	60.30	–	53.00
	s-c$_{[2]}$	17.20	0.011	18.60
	s-c$_{[3]}$	4.10	0.602	4.90
	–	18.40	–	23.50

4.2. Findings from single cell verification

The points of interest along the I–V characteristic, such as short-circuit current I_{SC}, MPP current I_{MPP}, MPP voltage V_{MPP} and fill-factor FF are plotted in Figs. 20a to 20d respectively.

(a) EL images with color-coded severity.

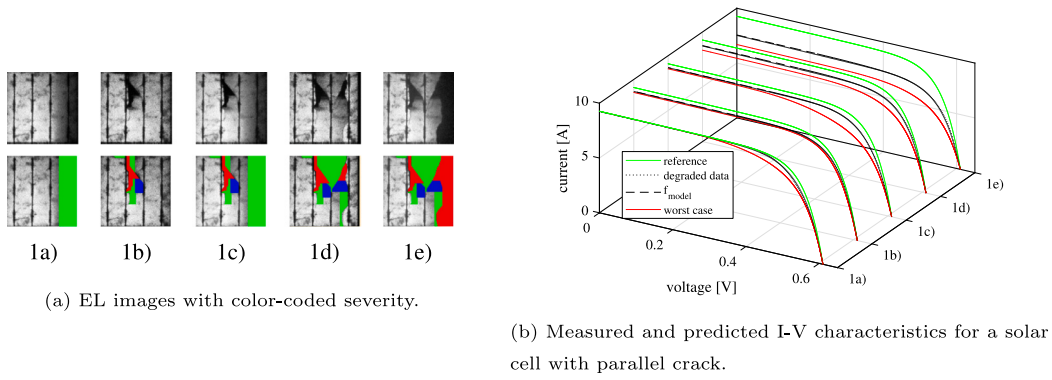(b) Measured and predicted I-V characteristics for a solar cell with parallel crack.

Fig. 17. EL images and I–V measurements of parallel cracks. (For interpretation of the references to color in this figure legend, the reader is referred to the web version of this article.)

(a) EL images with color-coded severity.

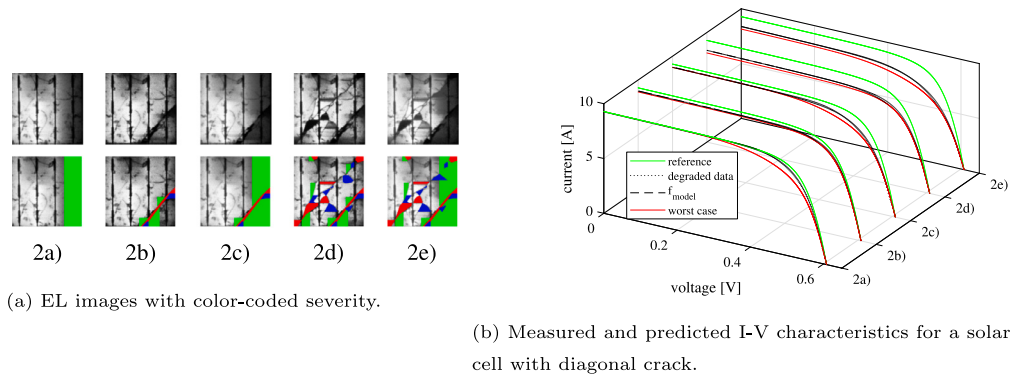(b) Measured and predicted I-V characteristics for a solar cell with diagonal crack.

Fig. 18. EL images and I–V measurements of diagonal cracks. (For interpretation of the references to color in this figure legend, the reader is referred to the web version of this article.)

(a) EL images with color-coded severity.

(b) Measured and predicted I-V characteristics for a solar cell with lateral crack.
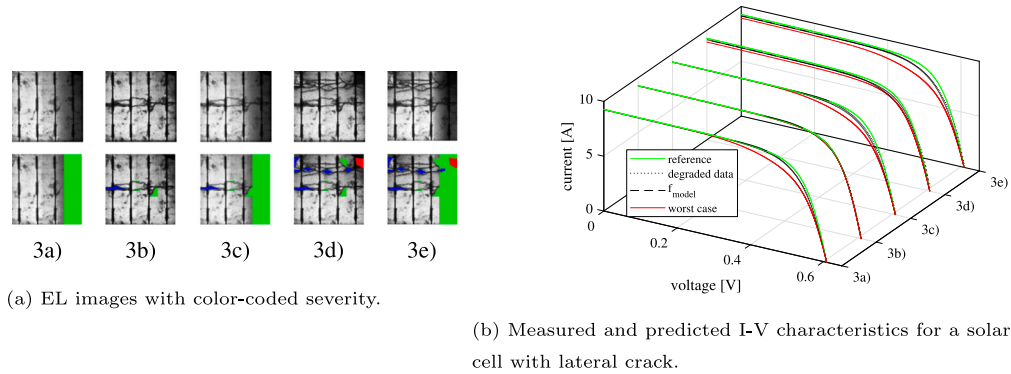
Fig. 19. EL images and I–V measurements of lateral cracks. (For interpretation of the references to color in this figure legend, the reader is referred to the web version of this article.)

The following conclusions are drawn:

- The proposed model well documents the changes due to observed degradation. As seen in Figs. 17b, 18b and 19b the model is capable of fitting the degraded I–V characteristic as further detailed by points of interest in Fig. 20.
- Tables 5–7 tabulated the identified parameter values $w_{[1]}$, $w_{[2]}$ and $w_{[3]}$ and compare them with w_{expect}, which is abstracted from Figs. 17a, 18a and 19a. The comparison shows the identified parameters are in proximity of the expected affected area.
- The identified parameter value $R_{x[2]}$ related to mild degradation is consistent across all tests. The $R_{x[3]}$ shows slight inconsistency, which is attributed to the existence of intermediate conductive interfaces within complex cracks, which the $R_{x[3]}$ represents.

The testing shows that a geometrical criterion applied to an EL image is sufficient to derive an equivalent circuit model representing sub-cell level degradation of solar cells. The regression performed by RJGGA, which requires the bounds $\{\theta_{lower}, \theta_{upper}\}$, where the θ_{lower} is estimated from the EL image, is capable of reaching suitable $\theta_{solution}$.

4.3. PV panel verification

The proposed model and regression method is tested on data of four crystalline panels. Compared to single cell verification, the focus is on approximation of the degradation observed in EL image by clustering of similarly degraded cells into Super-cells and limiting the number of sub-cells to 2 per Super-cell. The tested panels represent mono-crystalline and poly-crystalline categories at different ages and cracks
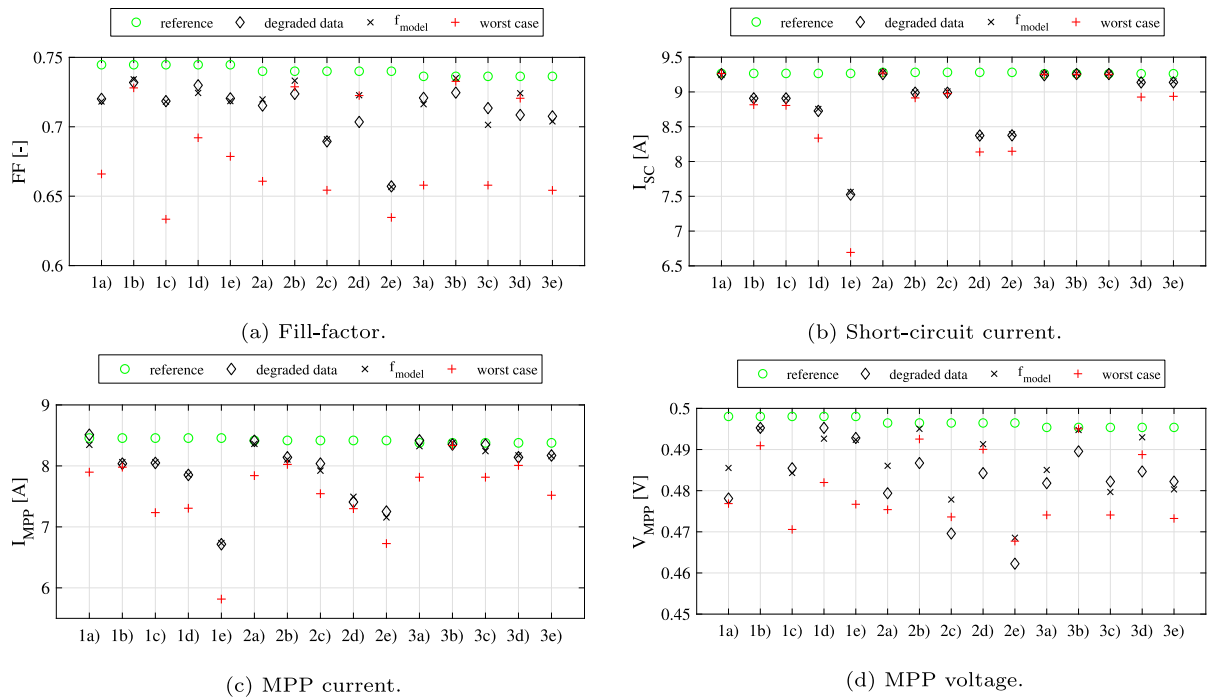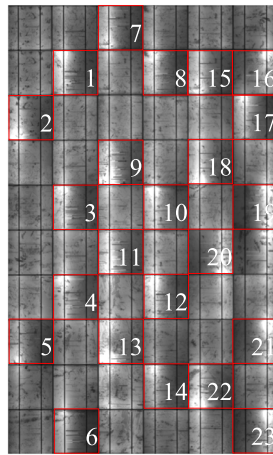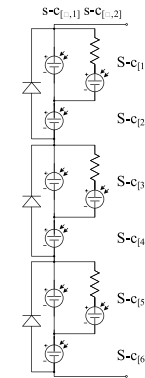
(a) Fill-factor.

(b) Short-circuit current.

(c) MPP current.

(d) MPP voltage.

Fig. 20. Points of interest along I–V characteristics for cases 1, 2 and 3.

(a) EL image.

(b) Equivalent circuit model f_{model}.

Fig. 21. Case 1: Mono-crystalline PV panel with interconnect failures.

and interconnect failure modes, 3 of them are measured by mobile test-bed and 1 in laboratory conditions.

The laboratory measurement includes data prior to degradation (reference state) and after the degradation. The laboratory conditions are close to STC conditions.

The mobile test-bed measurements do not include the reference state. Therefore, a single-diode model parameters I_{ph}, V_t, I_0 and R_s are identified using *PVID* (PhotoVoltaic IDentification) (Cannizzaro et al., 2014) based on datasheet values I_{SC}, I_{MPP}, V_{OC} and V_{MPP}. The identified parameters exclude the parameter R_{sh}, as the datasheet information is insufficient to calculate it. The estimation of R_{sh} and the second-diode parameters V_{t2} and I_{02} is discussed below.

The test-bed measurements were performed at temperature $T \approx 17$ [°C] and irradiation 850 [W/m^2] and corrected according to Standard IEC60891. Despite the correction, the Standard IEC60891 does not consider the physical phenomena within the semiconductor p–n junction,

but rather scales the I–V characteristic to approximate I_{SC} and V_{OC} at STC. The consequence of such correction is seen in the degraded data in Sections 4.3.2 (Fig. 24) and 4.3.4 (Fig. 28), where the linear sections of the I–V characteristic are almost horizontal, implying high value of R_{sh}. The laboratory measurements performed at STC, Section 4.3.1 (Fig. 22), show a slope, implying lower values of R_{sh}. This observation and the known inverse relation of R_{sh} with temperature and irradiation from Eqs. (13), we estimate the value of R_{sh} in reference state to be 120 [Ω] and 30 [Ω] for mono- and poly-crystalline solar cell respectively.

The second diode parameters are assumed $V_{t2} = V_{t1} \times 2$ and $I_{02} = I_{01} \times 10^{-1}$, which is in accordance with trends observed in Yahya-Khotbehsara and Shahhoseini (2018).

The reverse bias parameters are drawn from literature (Batzelis et al., 2014; Bishop, 1988), where the parameters take the values: $a = 0.10$ [–], $m = 3$ [–] and $V_{br} = -20$ [V].

Table 6
Parameters of the equivalent circuit model f_{model} for single cell with diagonal crack.

		w [%]	R_x [Ω]	w_{expect} [%]
S-c$_{(2a)}$	s-c$_{[1]}$	75.00	–	75.00
	s-c$_{[2]}$	25.00	**0.020**	25.00
S-c$_{(2b)}$	s-c$_{[1]}$	**89.30**	–	92.90
	s-c$_{[2]}$	**6.70**	**0.030**	4.20
	s-c$_{[3]}$	**1.00**	**6.281**	1.00
	–	1.90	–	1.90
S-c$_{(2c)}$	s-c$_{[1]}$	**69.50**	–	71.10
	s-c$_{[2]}$	**25.80**	**0.030**	26.10
	s-c$_{[3]}$	**2.80**	**1.295**	1.00
	–	1.90	–	1.80
S-c$_{(2d)}$	s-c$_{[1]}$	**78.00**	–	79.00
	s-c$_{[2]}$	**12.00**	**0.040**	8.00
	s-c$_{[3]}$	**2.00**	**4.967**	5.40
	–	8.00	–	7.60
S-c$_{(2e)}$	s-c$_{[1]}$	**61.60**	–	60.10
	s-c$_{[2]}$	**26.60**	**0.049**	26.90
	s-c$_{[3]}$	**3.00**	**2.608**	5.40
	–	8.80	–	7.60

Table 7
Parameters of the equivalent circuit model f_{model} for single cell with lateral crack.

		w [%]	R_x [Ω]	w_{expect} [%]
S-c$_{(3a)}$	s-c$_{[1]}$	75.00	–	75.00
	s-c$_{[2]}$	25.00	**0.021**	25.00
S-c$_{(3b)}$	s-c$_{[1]}$	**99.00**	–	98.40
	s-c$_{[2]}$	**0.05**	**0.035**	0.90
	s-c$_{[3]}$	**0.05**	**2.214**	0.70
	–	0.00	–	0.00
S-c$_{(3c)}$	s-c$_{[1]}$	**75.00**	–	73.70
	s-c$_{[2]}$	**25.00**	**0.032**	25.60
	s-c$_{[3]}$	**0.00**	**0.00**	0.70
	–	0.00	–	0.00
S-c$_{(3d)}$	s-c$_{[1]}$	**94.10**	–	94.20
	s-c$_{[2]}$	**1.90**	**0.025**	1.60
	s-c$_{[3]}$	**2.70**	**0.843**	2.90
	–	1.30	–	1.30
S-c$_{(3e)}$	s-c$_{[1]}$	**71.70**	–	71.30
	s-c$_{[2]}$	**24.10**	**0.026**	24.50
	s-c$_{[3]}$	**2.90**	**0.401**	2.90
	–	1.30	–	1.30

Table 8
Reference double-diode model parameters for a single solar cell.

I_{ph} [A]	I_{01} [A]	V_{t1} [V]	I_{02} [A]	V_{t2} [V]	R_s [Ω]	R_{sh} [Ω]
8.591	4.283^{-10}	0.0262	4.283^{-11}	0.0524	0.0058	6

The regression is performed on parameters $\theta = \{w_{[i,j]}, R_{x[i,j]}\}$ that are highlighted in **bold** within Tables 9, 11, 13 and 15. Other parameters are kept constant.

The RJGGA parameters K, P and number of iterations until convergence are set to 50, 20 and 500 respectively.

4.3.1. Case 1: interconnect failures

A new poly-crystalline PV panel with intentionally damaged interconnect is tested. The EL image accompanied with electric equivalent circuit model is shown in Fig. 21. The cells marked 1 to 6 are represented by S-c$_{[1]}$, cells 7 to 11 by S-c$_{[3]}$ and cells 12 to 19 by S-c$_{[5]}$.

The reference parameters of a single cell are tabulated in Table 8.

The parameters of the model depicted in Fig. 21b are tabulated in Table 9.

The reference state and the degraded I–V characteristic fitted with the proposed model is depicted in Fig. 22.

Table 9
Parameters of equivalent circuit model f_{model} in Fig. 21b.

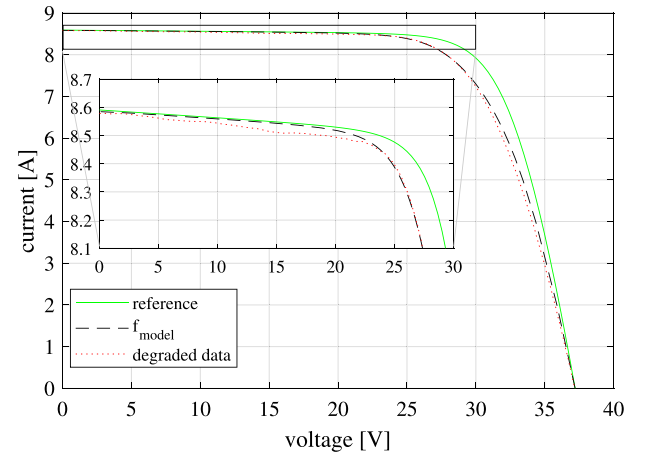|		w [%]	R_x [Ω]	h [cell]
S-c$_{[1]}$	s-c$_{[1,1]}$	50.00	–	6
	s-c$_{[1,2]}$	50.00	**0.168**	
S-c$_{[2]}$	s-c$_{[2,1]}$	100.0	–	14
S-c$_{[3]}$	s-c$_{[3,1]}$	50.00	–	8
	s-c$_{[3,2]}$	50.00	**0.224**	
S-c$_{[4]}$	s-c$_{[4,1]}$	100.0	–	12
S-c$_{[5]}$	s-c$_{[5,1]}$	50.00	–	9
	s-c$_{[5,2]}$	50.00	**0.252**	
S-c$_{[6]}$	s-c$_{[6,1]}$	100.0	–	11

Fig. 22. Comparison of measured I–V characteristic and I–V characteristic predicted by f_{model}.

Table 10
Reference double-diode model parameters for a single solar cell.

I_{ph} [A]	I_{01} [A]	V_{t1} [V]	I_{02} [A]	V_{t2} [V]	R_s [Ω]	R_{sh} [Ω]
8.932	4.162^{-10}	0.0277	4.162^{-11}	0.0555	0.0065	120

Regressing the f_{model} to the I–V characteristic degraded by severed interconnect bus-bars reveals the distributed resistance in Table 9. Reversing the clustering of Super-cells by dividing the identified resistance R_x with the according number of cells h, the resistance introduced by a severed bus-bar by single physical cell with 2 bus-bars is $R_x = 0.028$ [Ω]. This is in line with findings in experimental single cell verification, where single severed bus-bar for cell with 4 bus-bars caused $R_x \approx 0.020$ [Ω]. Further, the result is consistent with findings in Annigoni et al. (2019), where the resistance introduced by severed bus-bar is $R_x \approx 0.026$ [Ω] for a cell with 3 bus-bars.

### 4.3.2. Case 2: mobile test-bed measurement

A less than 1 year old mono-crystalline PV panel with visible cracks across 4 cells is tested. The EL image accompanied with electric equivalent circuit model is shown in Fig. 23. The cell marked 1 is represented by S-c$_{[1]}$, cell 2 is represented by S-c$_{[2]}$, cell 3 is represented by S-c$_{[5]}$ and cell 4 is represented by S-c$_{[6]}$.

The reference parameters of a single cell are tabulated in Table 10.

The parameters of the model depicted in Fig. 23b are tabulated in Table 11.

The reference state and the degraded I–V characteristic fitted with the proposed model is depicted in Fig. 24.

The matching I–V characteristics in Fig. 24 show the model well describes the degradation of a new PV panel with cracks across 4 cells. The missing area of the cracked solar cells restricts the amount of current that the cells are capable of passing, thus yielding lower
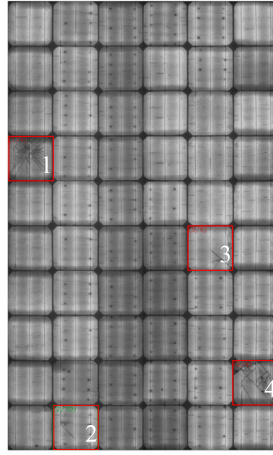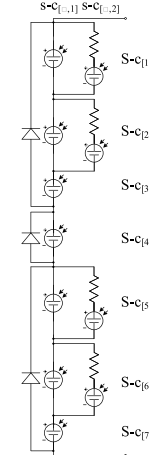
(a) EL image.   (b) Equivalent circuit model f_{model}.

Fig. 23. Case 2: Mono-crystalline PV panel with several cracked cells.

Table 11

Parameters of the equivalent circuit model f_{model} in Fig. 23b.

		w [%]	R_x [Ω]	h [cell]
S-c$_{[1]}$	s-c$_{[1,1]}$	66.00	–	1
	s-c$_{[1,2]}$	**31.93**	**0.189**	
S-c$_{[2]}$	s-c$_{[2,1]}$	92.50	–	1
	s-c$_{[2,2]}$	7.50	0.020	
S-c$_{[3]}$	s-c$_{[3,1]}$	100.0	–	18
S-c$_{[4]}$	s-c$_{[4,1]}$	100.0	–	20
S-c$_{[5]}$	s-c$_{[5,1]}$	90.00	–	1
	s-c$_{[5,2]}$	**6.36**	**0.059**	
S-c$_{[6]}$	s-c$_{[6,1]}$	80.00	–	1
	s-c$_{[6,2]}$	**16.29**	**0.162**	
S-c$_{[7]}$	s-c$_{[7,1]}$	100.0	–	18

Table 12

Reference double-diode model parameters for a single solar cell.

I_{ph} [A]	I_{01} [A]	V_{t1} [V]	I_{02} [A]	V_{t2} [V]	R_s [Ω]	R_{sh} [Ω]
8.591	2.023^{-8}	0.0320	2.023^{-9}	0.0640	0.0065	30

4.3.3. Case 3: mobile test-bed measurement

Further, an approximately 15 years old poly-crystalline panel is investigated. The EL image accompanied with electric equivalent circuit model is shown in Fig. 25. Although the EL image depicts only 3 cracked solar cells, the observed loss in power output is $\Delta P = 17.74$ [W]. Such loss cannot be accounted for by the 3 damaged solar cells, where each cell produces only up to 4.08 [W]. Therefore, the model is used to investigate an approximate degradation that causes the significant drop in power ΔP without the information from EL image.

Super-cell $S\text{-}c_{[4]}$ and $S\text{-}c_{[8]}$ represent cell number 1 and 3 respectively, with observed 1 [%] missing area. The rest of the Super-cells represent all other 58 physical solar cells, grouped into similarly sized groups of 6 to 7 solar cells as seen in Table 13.

The reference parameters for a single cell are tabulated in Table 12.

The parameters of the model depicted in Fig. 25b are tabulated in Table 13.

The reference state and the degraded I–V characteristic fitted with the proposed model is depicted in Fig. 26.

Although, the results do not represent the exact internal state of the solar cells, the following is observed. Table 13 shows a high probability of distributed resistive losses, as the cells in the first sub-string represented by $S\text{-}c_{[1-3]}$ show distributed resistance of 0.056 [Ω] per physical cell across 40 [%] of area for 6 cells (sub-cell $s\text{-}c_{[1,2]}$), 0.075 [Ω] per physical cell across 30 [%] of area for 7 cells (sub-cell $s\text{-}c_{[2,2]}$) and 0.114 [Ω] per physical cell over 20 [%] of area for 6 cells (sub-cell $s\text{-}c_{[3,2]}$). The value of distributed resistance per physical cell is significantly higher than the 0.028 [Ω] per physical cell for Laboratory measurement with interconnect failures. Therefore, despite the convergence of the regression method, the abstracted parameters are inconclusive on exact nature of degradation, as the current result cannot fully justify such high distributed resistance per cell without significant faults observed in the EL image.

4.3.4. Case 4: mobile test-bed measurement

Lastly, a less than 3 years old mono-crystalline PV panel is investigated. The EL image in Fig. 27 shows excessive damage, where 14 cells are significantly cracked.
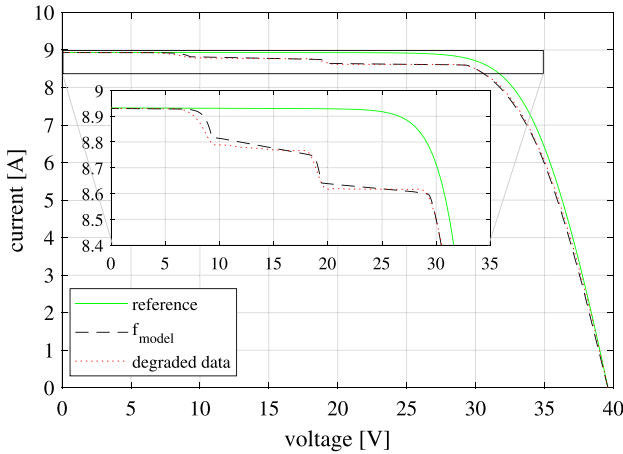
Fig. 24. Comparison of measured I–V characteristic and I–V characteristic predicted by f_{model}.

value of I_{SC}. This causes an early conduction of by-pass diodes, which appears as steep steps within the linear region of the degraded I–V characteristic. Although, the misalignment of I_{SC} among cells is relatively common, the model identifies missing area of 3.71 [%] for $S\text{-}c_{[6]}$ (cell number 4 in Fig. 23a), which is unlikely to originate as manufacturing artifact.
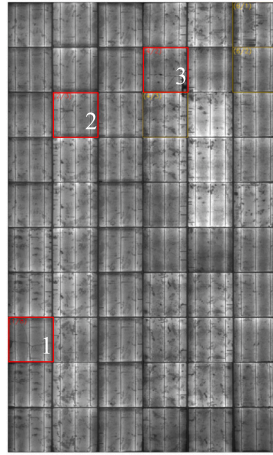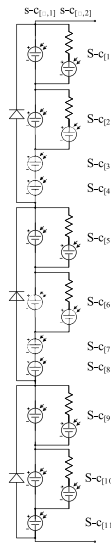
(a) EL image.

(b) Equivalent circuit model f_{model}.

Fig. 25. Case 3: Poly-crystalline PV panel with several cracked cells.

Table 13
Parameters of the equivalent circuit model f_{model} in Fig. 25b.

		w [%]	R_x [Ω]	h [cell]
S-c[1]	s-c[1,1]	60.00	–	6
	s-c[1,2]	40.00	**0.338**	
S-c[2]	s-c[2,1]	70.00	–	7
	s-c[2,2]	30.00	**0.526**	
S-c[3]	s-c[3,1]	80.00	–	6
	s-c[3,2]	20.00	**0.689**	
S-c[4]	s-c[4,1]	99.00	–	1
S-c[5]	s-c[5,1]	90.00	–	6
	s-c[5,2]	10.00	**1.981**	
S-c[6]	s-c[6,1]	95.00	–	7
	s-c[6,2]	5.00	**9.981**	
S-c[7]	s-c[7,1]	97.50	–	6
	s-c[7,2]	2.50	**8.251**	
S-c[8]	s-c[8,1]	99.00	–	1
S-c[9]	s-c[1,1]	97.00	–	6
	s-c[1,2]	3.00	**6.973**	
S-c[10]	s-c[2,1]	98.00	–	7
	s-c[2,2]	2.00	**6.351**	
S-c[11]	s-c[3,1]	98.50	–	7
	s-c[3,2]	1.50	**7.168**	

Table 14
Reference double-diode model parameters for a single solar cell.

I_{ph} [A]	I_{01} [A]	V_{t1} [V]	I_{02} [A]	V_{t2} [V]	R_s [Ω]	R_{sh} [Ω]
8.932	4.162^{-10}	0.0277	4.162^{-11}	0.0555	0.0065	120

Super-cell $S\text{-}c_{[1]}$ represents cells 2, 4 and 5. Super-cell $S\text{-}c_{[2]}$ represents cells 1 and 3. Super-cell $S\text{-}c_{[4]}$ represents cells 6 to 8 and Super-cell $S\text{-}c_{[6]}$ represents cells 9 to 14.

The reference parameters for a single cell are tabulated in Table 14.

The parameters of the model depicted in Fig. 27b are tabulated in Table 15.

The reference state and the degraded I–V characteristic fitted with the proposed model is depicted in Fig. 28. The f^*_{model} depicts prediction by equivalent circuit model with modified parameter V_{br}.
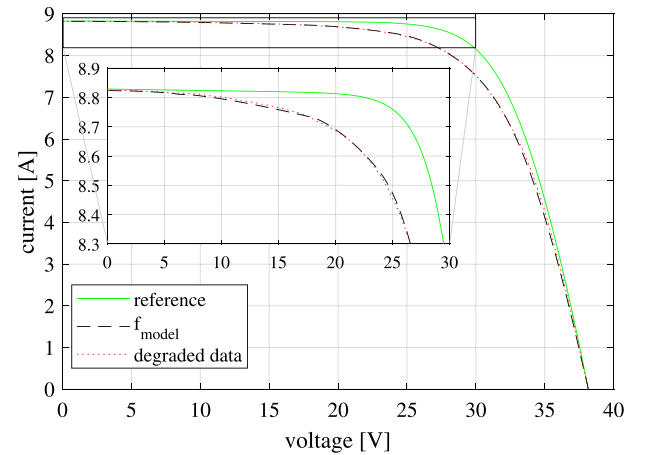

Fig. 26. Comparison of measured I–V characteristic and I–V characteristic predicted by f_{model}.

Table 15
Parameters of the equivalent circuit model f_{model} in Fig. 27b.

		w [%]	R_x [Ω]	h [cell]
S-c[1]*	s-c[1,1]	**97.90**	–	3
S-c[2]	s-c[2,1]	70.00	–	2
	s-c[2,2]	**29.97**	**0.023**	
S-c[3]	s-c[3,1]	100.0	–	15
S-c[4]	s-c[4,1]	70.00	–	5
	s-c[4,2]	**29.93**	**0.086**	
S-c[5]	s-c[5,1]	100.0	–	15
S-c[6]	s-c[6,1]	70.00	–	6
	s-c[6,2]	**27.45**	**0.098**	
S-c[7]	s-c[7,1]	100.0	–	14

In this case an anomaly is observed, where the convexity of the measured I–V characteristic changes unexpectedly. There are only 2 sources of convexity in a PV panel for the I. and IV. quadrant:

• By-pass diode
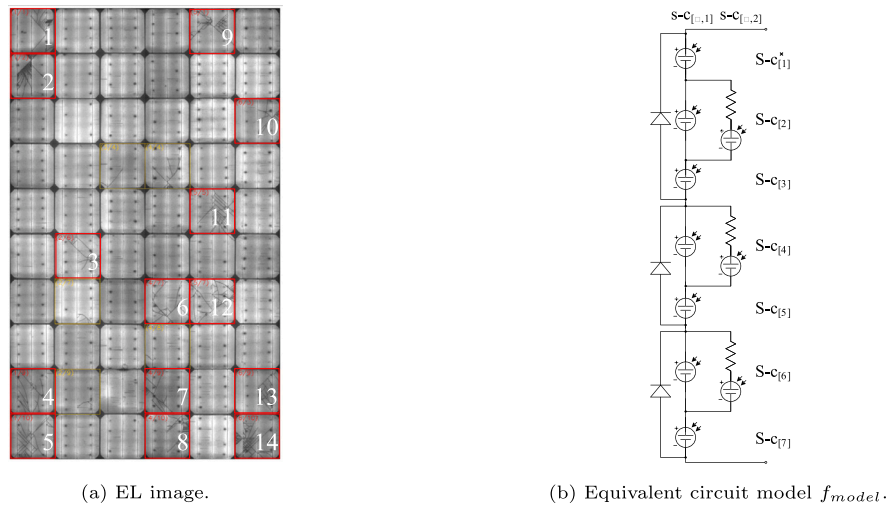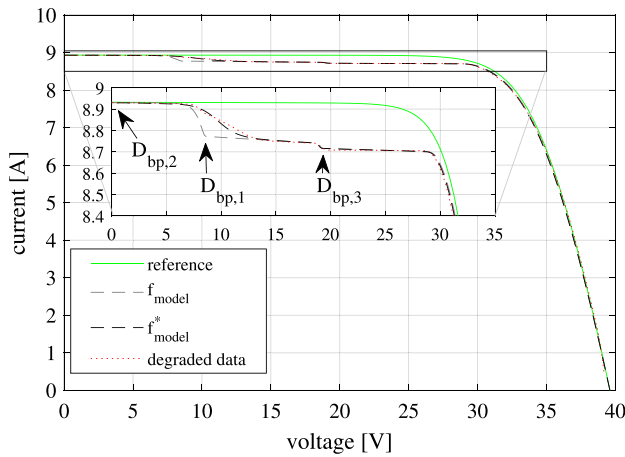• Reverse-bias characteristic of a solar cell

(a) EL image.

(b) Equivalent circuit model f_{model}.

Fig. 27. Case 4: Mono-crystalline PV panel with extensive degradation.

Fig. 28. Comparison of measured I–V characteristic and I–V characteristic predicted by f_{model}.

Fig. 29. Sub-string I–V characteristics depicting by-pass diode conduction.

By-pass diode is designed to conduct the excessive current that otherwise causes degraded cells to reach avalanche breakdown. In this case, a rise in current is observed at voltage 13 [V]. At this voltage, the voltage across the by-pass diode is still positive, thus the diode is not conducting any current.

Therefore, the changes of solar cells are investigated. The convexity within the reverse-bias characteristic is significantly influenced by the parameter V_{br}. The value $V_{br} = -10$ [V] for Super-cell $S\text{-}c^*_{[1]}$ causes the affected cells approach the avalanche breakdown sooner than the by-pass diode starts to conduct. The Fig. 29 illustrates the sub-panel I–V characteristics of sub-strings with by-pass diodes $D_{bp,1-3}$. The conduction of by-pass diodes is marked by arrows which correspond to the arrows in Fig. 28.

As observed in Fig. 29, the model provides an insight into a sub-string level of the degraded PV panel. It reveals that one or several cells in the leftmost sub-string are potentially close to the avalanche breakdown before the by-pass diode $D_{bp,1}$ conducts.

5. Conclusion

In this article, we propose a novel model for characterizing degradation at the sub-cell level of a PV panel. The model is an equivalent circuit model b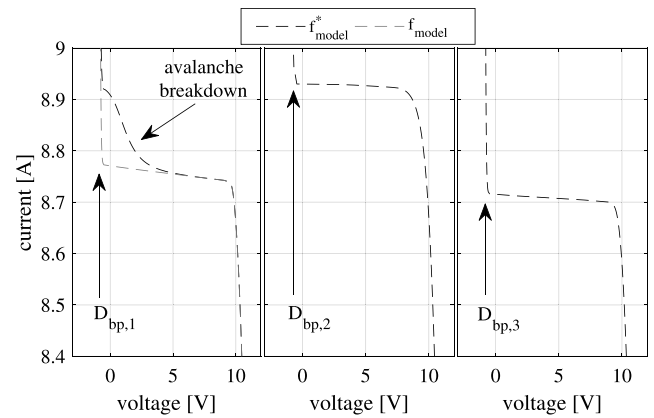ased on double-diode model extended by reverse-bias characteristic model. The parameters of these models are augmented to incorporate quantities related to degradation, such as affected area of a solar cell(s) and severity of the degradation.

Furthermore, a novel regression problem is proposed and solved by an Evolutionary Algorithm using Real-Jumping Gene Genetic Algorithm. The regression infers the parameters of the proposed model by merging information from EL image and degraded PV panel's I–V characteristic.

An integral part of the investigation is an analysis of EL image using geometrical criterion, which is originally proposed to estimate the impact of cracks. We experimentally verify the geometrical criterion and extend it to estimate the degradation due to interconnect failures. Though the estimation from the EL image alone is not sufficient to precisely infer the electrical properties of cracks and interconnect failures, it is sufficient to set the worst case scenario on electrical performance at the level of a single solar cell. The worst case estimate plays an essential role in the Evolutionary Algorithm search strategy, as the solution is required to exist between the reference state of the PV panel and the estimated worst case scenario.

The outcome of the proposed model and regression method is a set of parameters characterizing the defects at the sub-cell level of a PV panel. Such approach removes the requirement of disassembling the PV panel in order to measure the electrical properties of degraded solar cells. The non-intrusive property of the proposed approach is a basis for efficient large-scale diagnostics.

Furthermore, we show that the proposed method delivers acceptable results despite insufficient information from EL image or unknown degradation mode. In the first case, the model is used to identify potential distributed resistance across the PV panel (for instance due to corrosion on the back side of the PV panel, which is not visible in EL image). In the second case, the model is used to investigate probable divergence in the solar cell parameters, which may be caused by faulty manufacturing process (unusual reverse-bias characteristic of solar cells).

The proposed method is experimentally verified at the cell level by destructive testing and on a PV panel data obtained in laboratory conditions and from mobile test-bed. Since the model is based on widely adopted double-diode model, it is expected that the results can be replicated for other PV technologies, such as thin-film. The demonstrated flexibility of the model can also serve PV panels with different connection of solar cells or alternative connections of by-pass diodes.

Declaration of competing interest

The authors declare that they have no known competing financial interests or personal relationships that could have appeared to influence the work reported in this paper.

Acknowledgments

References

Annigoni, E., Virtuani, A., Levrat, J., Faes, A., Sculati-Meillaud, F., Despeisse, M., Ballif, C., 2019. Quantifying and modeling the impact of interconnection failures on the electrical performance of crystalline silicon photovoltaic modules. Prog. Photovolt., Res. Appl. http://dx.doi.org/10.1002/pip.3111.

Bastidas, J.D., Franco, E., Petrone, G., Ramos-Paja, C.A., Spagnuolo, G., 2013. A model of photovoltaic fields in mismatching conditions featuring an improved calculation speed. Electr. Power Syst. Res. http://dx.doi.org/10.1016/j.epsr.2012.10.020.

Batzelis, E.I., Routsolias, I.A., Papathanassiou, S.A., 2014. An explicit pv string model based on the lambert w function and simplified mpp expressions for operation under partial shading. IEEE Trans. Sustain. Energy http://dx.doi.org/10.1109/TSTE.2013.2282168.

Berardone, I., Corrado, M., Paggi, M., 2014. A generalized electric model for mono and polycrystalline silicon in the presence of cracks and random defects. In: Energy Procedia. http://dx.doi.org/10.1016/j.egypro.2014.08.005.

Bishop, J.W., 1988. Computer simulation of the effects of electrical mismatches in photovoltaic cell interconnection circuits. Solar Cells http://dx.doi.org/10.1016/0379-6787(88)90059-2.

Bosco, N., Silverman, T.J., Wohlgemuth, J., Kurtz, S., Inoue, M., Sakurai, K., Shioda, T., Zenkoh, H., Hirota, K., Miyashita, M., Tadanori, T., Suzuki, S., 2013. Evaluation of dynamic mechanical loading as an accelerated test method for ribbon fatigue. In: Conference Record of the IEEE Photovoltaic Specialists Conference. http://dx.doi.org/10.1109/PVSC.2013.6745128.

Cannizzaro, S., Di Piazza, M.C., Luna, M., Vitale, G., 2014. PVID: An interactive matlab application for parameter identification of complete and simplified single-diode PV models. In: 2014 IEEE 15th Workshop on Control and Modeling for Power Electronics, COMPEL 2014. http://dx.doi.org/10.1109/COMPEL.2014.6877152.

Chattopadhyay, S., Dubey, R., Bhaduri, S., Zachariah, S., Singh, H.K., Solanki, C.S., Kottantharayil, A., Shiradkar, N., Arora, B.M., Narasimhan, K.L., Vasi, J., 2018. Correlating infrared thermography with electrical degradation of pv modules inspected in all-india survey of photovoltaic module reliability 2016. IEEE J. Photovolt. http://dx.doi.org/10.1109/JPHOTOV.2018.2859780.

Chen, Y., Sun, Y., Meng, Z., 2018. An improved explicit double-diode model of solar cells: Fitness verification and parameter extraction. Energy Convers. Manage. http://dx.doi.org/10.1016/j.enconman.2018.05.035.

Dkhichi, F., Oukarfi, B., Fakkar, A., Belbounaguia, N., 2014. Parameter identification of solar cell model using levenberg-marquardt algorithm combined with simulated annealing. Sol. Energy http://dx.doi.org/10.1016/j.solener.2014.09.033.

Dubey, R., Chattopadhyay, S., Kuthanazhi, V., Kottantharayil, A., Singh Solanki, C., Arora, B.M., Narasimhan, K.L., Vasi, J., Bora, B., Singh, Y.K., Sastry, O.S., 2017. Comprehensive study of performance degradation of field-mounted photovoltaic modules in India. Energy Sci. Eng. http://dx.doi.org/10.1002/ese3.150.

Garaj, M., Hong, K.Y., Chung, H.S.H., lun Lo, A.W., Wang, H., 2020. Diagnostic module for series-connected photovoltaic panels. Sol. Energy http://dx.doi.org/10.1016/j.solener.2019.12.019.

Gong, W., Cai, Z., 2013. Parameter extraction of solar cell models using repaired adaptive differential evolution. Sol. Energy http://dx.doi.org/10.1016/j.solener.2013.05.007.

Horowitz, C.A., 2016. Paris agreement. Int. Legal Mater. http://dx.doi.org/10.1017/s0020782900004253.

Humada, A.M., Hojabri, M., Mekhilef, S., Hamada, H.M., 2016. Solar cell parameters extraction based on single and double-diode models: A review. http://dx.doi.org/10.1016/j.rser.2015.11.051.

Ishaque, K., Salam, Z., Mekhilef, S., Shamsudin, A., 2012. Parameter extraction of solar photovoltaic modules using penalty-based differential evolution. Appl. Energy http://dx.doi.org/10.1016/j.apenergy.2012.05.017.

Jeong, J.S., Park, N., Han, C., 2012. Field failure mechanism study of solder interconnection for crystalline silicon photovoltaic module. Microelectron. Reliab. http://dx.doi.org/10.1016/j.microrel.2012.06.027.

Jordan, D.C., Silverman, T.J., Wohlgemuth, J.H., Kurtz, S.R., VanSant, K.T., 2017. Photovoltaic failure and degradation modes. Prog. Photovolt., Res. Appl. http://dx.doi.org/10.1002/pip.2866.

Kntges, M., Kunze, I., Kajari-Schrder, S., Breitenmoser, X., Bjørneklett, B., 2011. The risk of power loss in crystalline silicon based photovoltaic modules due to micro-cracks. Sol. Energy Mater. Sol. Cells http://dx.doi.org/10.1016/j.solmat.2010.10.034.

Macabebe, E.Q.B., Sheppard, C.J., van Dyk, E.E., 2011. Parameter extraction from I-V characteristics of PV devices. Sol. Energy http://dx.doi.org/10.1016/j.solener.2010.11.005.

Nehme, B.F., Akiki, T.K., Naamane, A., M'Sirdi, N.K., 2017. Real-time thermoelectrical model of PV panels for degradation assessment. IEEE J. Photovolt. http://dx.doi.org/10.1109/JPHOTOV.2017.2711430.

Orozco-Gutierrez, M.L., Ramirez-Scarpetta, J.M., Spagnuolo, G., Ramos-Paja, C.A., 2013. A technique for mismatched PV array simulation. Renew. Energy http://dx.doi.org/10.1016/j.renene.2013.01.009.

Paggi, M., Berardone, I., Infuso, A., Corrado, M., 2014. Fatigue degradation and electric recovery in Silicon solar cells embedded in photovoltaic modules. Sci. Rep. http://dx.doi.org/10.1038/srep04506.

Paggi, M., Corrado, M., Berardone, I., 2016. A global/local approach for the prediction of the electric response of cracked solar cells in photovoltaic modules under the action of mechanical loads. Eng. Fract. Mech. http://dx.doi.org/10.1016/j.engfracmech.2016.01.018.

Petrone, G., Spagnuolo, G., Vitelli, M., 2007. Analytical model of mismatched photovoltaic fields by means of Lambert W-function. Sol. Energy Mater. Sol. Cells http://dx.doi.org/10.1016/j.solmat.2007.05.021.

Pletzer, T.M., Van Mölken, J.I., Rißland, S., Breitenstein, O., Knoch, J., 2015. Influence of cracks on the local current-voltage parameters of silicon solar cells. Prog. Photovolt., Res. Appl. http://dx.doi.org/10.1002/pip.2443.

Qing, X., Sun, H., Feng, X., Chung, C.Y., 2017. Submodule-based modeling and simulation of a series-parallel photovoltaic array under mismatch conditions. IEEE J. Photovolt. http://dx.doi.org/10.1109/JPHOTOV.2017.2746265.

REN21, 2020. Renewables 2020 Global Status Report. Technical Report.

Rossi, D., Omana, M., Giaffreda, D., Metra, C., 2015. Modeling and detection of hotspot in shaded photovoltaic cells. IEEE Trans. Very Large Scale Integr. (VLSI) Syst. http://dx.doi.org/10.1109/TVLSI.2014.2333064.

Sharma, V., Chandel, S.S., 2016. A novel study for determining early life degradation of multi-crystalline-silicon photovoltaic modules observed in western Himalayan Indian climatic conditions. Sol. Energy http://dx.doi.org/10.1016/j.solener.2016.04.023.

Silva, E.A., Bradaschia, F., Cavalcanti, M.C., Nascimento, A.J., Michels, L., Pietta, L.P., 2017. An eight-parameter adaptive model for the single diode equivalent circuit based on the photovoltaic module's physics. IEEE J. Photovolt. http://dx.doi.org/10.1109/JPHOTOV.2017.2703778.

Singh, S., Agrawal, S., Tiwari, A., Al-Helal, I.M., Avasthi, D.V., 2015. Modeling and parameter optimization of hybrid single channel photovoltaic thermal module using genetic algorithms. Sol. Energy http://dx.doi.org/10.1016/j.solener.2014.12.031.

Spataru, S., Hacke, P., Sera, D., 2018. Automatic Detection of Inactive Solar Cell Cracks in Electroluminescence Images. http://dx.doi.org/10.1109/pvsc.2017.8366106.

Van Mölken, J.I., Yusufoğlu, U.A., Safiei, A., Windgassen, H., Khandelwal, R., Pletzer, T.M., Kurza, H., 2012. Impact of micro-cracks on the degradation of solar cell performance based on two-diode model parameters. In: Energy Procedia. http://dx.doi.org/10.1016/j.egypro.2012.07.046.

Wu, X., Bliss, M., Sinha, A., Betts, T.R., Gupta, R., Gottschalg, R., 2015. Accelerated spatially resolved electrical simulation of photovoltaic devices using photovoltaic-oriented nodal analysis. IEEE Trans. Electron Devices http://dx.doi.org/10.1109/TED.2015.2409058.

Yahya-Khotbehsara, A., Shahhoseini, A., 2018. A fast modeling of the double-diode model for PV modules using combined analytical and numerical approach. Sol. Energy http://dx.doi.org/10.1016/j.solener.2018.01.047.